Astronomy & Astrophysics manuscript no. ms_printer_v7
January 27, 2022

VEGAS-SSS. A VST survey of Elliptical Galaxies in the Southern hemisphere: analysis of Small Stellar Systems

Testing the methodology on the globular cluster system in NGC 3115

Michele Cantiello[1], Massimo Capaccioli[2,3], Nicola Napolitano[3], Aniello Grado[3], Luca Limatola[3], Maurizio Paolillo[2,4], Enrica Iodice[3], Aaron J. Romanowsky[5,6], Duncan A. Forbes[7], Gabriella Raimondo[1], Marilena Spavone[3], Francesco La Barbera[3], Thomas H. Puzia[8,9], and Pietro Schipani[3]

[1] INAF Osservatorio Astr. di Teramo, via Maggini,-64100, Teramo, Italy e-mail: cantiello@oa-teramo.inaf.it
[2] Dip. di Fisica, Universitá di Napoli Federico II, C.U. di Monte Sant'Angelo, Via Cintia, 80126 Naples, Italy
[3] INAF Osservatorio Astr. di Capodimonte Napoli, Salita Moiariello, 80131, Napoli, Italy
[4] Agenzia Spaziale Italiana - Science Data Center, Via del Politecnico snc, 00133 Roma, Italy
[5] University of California Observatories, 1156 High Street, Santa Cruz, CA 95064, USA
[6] Department of Physics and Astronomy, San José State University, One Washington Square, San Jose, CA 95192, USA
[7] Centre for Astrophysics & Supercomputing, Swinburne University, Hawthorn, VIC 3122, Australia
[8] Institute of Astrophysics, Pontificia Universidad Católica de Chile, Avenida Vicuña Mackenna 4860, Macul, 7820436, Santiago, Chile
[9] National Research Council Canada, Herzberg Institute of Astrophysics, 5071 West Saanich Road, Victoria, BC V9E 2E7, Canada

ABSTRACT

We present a study of globular clusters (GCs) and other small stellar systems (SSSs) in the field of NGC 3115, observed as part of the ongoing wide-field imaging survey VEGAS, carried out with the 2.6m VST telescope. We use deep g and i observations of NGC 3115, a well-studied lenticular galaxy with excellent scientific literature. This is fundamental for testing the methodologies, verifying the results, and probing the capabilities of the VEGAS-SSS. Leveraging the large field of view of VST allows us to carry out an accurate study of the distribution and properties of SSSs as a function of galactocentric distance, well beyond ~ 20 galaxy effective radii, in a way not often possible. Our analysis of colours, magnitudes and sizes of SSS candidates confirms the results from the existing studies, some of which carried out with 8-10m class telescopes, and further extends them to previously unreached galactocentric distances, with comparable accuracy. In particular, we find a colour bimodality for the GC population and a de Vaucouleurs $r^{1/4}$ profile for the surface density of GCs as for the galaxy light profile. The radial colour gradient of blue and red GCs already found, e.g., by the SLUGGS survey with Subaru and Keck data, is further extended out to the largest galactocentric radii inspected, ~ 65 kpc. In addition, the surface density profiles of blue and red GCs taken separately are well approximated by a $r^{1/4}$ density profile, with the fraction of blue GCs being slightly larger at larger radii. We do not find hints of a trend for the red GC subpopulation and for the GC turnover magnitude to vary with radius, but we observe a ~ 0.2 mag difference in the turnover magnitude of the blue and red GCs subpopulations. Finally, inspecting SSS sizes and colours we obtained a list of ultracompact dwarf galaxies and GC candidates suitable for future spectroscopic follow-up. In conclusion, the present study shows *i*) the reliability of the methodologies developed to study SSSs in the field of bright early-type galaxies; and *ii*) the great potential of the VEGAS survey to produce original results on SSSs science, mainly thanks to the wide-field imaging adopted.

Key words. Galaxies: star clusters: general – Galaxies: stellar content – Galaxies: statistics – Galaxies: individual: NGC 3115 – Surveys – Catalogs

1. Introduction

The study of the properties of old star clusters in and around galaxies is one of the keystones for understanding the formation and evolution of galaxies (Ashman & Zepf 1992; Forbes et al. 1997; Côté et al. 1998; Brodie & Strader 2006; Tonini 2013). Because of the relative ease to detect them out to large galactocentric distances, and of the lower complexity of their host stellar populations with respect to massive galaxies, star clusters provide an accurate and relatively straightforward tool to unveil the mechanisms that produced the present distribution and evolutionary properties of stars in the host galaxy.

The surroundings of massive galaxies are populated by a zoo of small stellar systems (SSSs hereafter): globular clusters (GCs), extended clusters (ECs), ultra compact dwarfs (UCDs), dwarf spheroidals (dSphs), dwarf ellipticals (dEs), compact ellipticals (cE) etc. (see, e.g., Forbes et al. 2013, and references therein). The characteristic magnitude, colours and half-light radii for some SSS classes are given in Table 1. We emphasize that

the distinction between the different SSS types is sometimes not trivial, and somewhat arbitrary, due to the lack of sharp distinction between the classes of SSSs as revealed, for example, by the scaling relations of mass, radius, luminosity, central surface brightness, or velocity dispersion (Drinkwater et al. 2004; Misgeld & Hilker 2011; Chiboucas et al. 2011; McConnachie 2012). A natural explanation to the lack of clear class-boundaries is that there is not any. Indeed, the transformation processes occurring in dense environments may cause the disruption or transformation of massive SSSs, littering the galaxy field with the remains of disrupted system: low mass SSSs, stellar streams, etc. (Bassino et al. 1994; West et al. 1995; D'Abrusco et al. 2013, 2014).

Characterizing the properties of the wealth of SSSs in the potential well of the host galaxy is fundamental for the understanding of their origin, and is an important tool for gauging the growth of the galaxy and, more in general, of cosmic structures.

In this context, the present study is dedicated to the analysis of SSSs in NGC 3115, and is the first of a series aimed at analyzing SSSs in bright early-type galaxies, observed as part of the ongoing imaging VST survey VEGAS ("VST survey of Elliptical Galaxies in the Southern hemisphere", distributed over many semesters; GTO-INAF program, P.I. Massimo Capaccioli).

An overview of VEGAS, and of its scientific aims, is presented in Capaccioli et al. (2014). At completion, the survey will collect detailed photometric information of ~ 100 bright early-type galaxies, to study the galaxy light distribution out to $\sim$15-20 effective radii. These galaxy regions are still almost unexplored in the CCD era, mainly because of the difficulties posed by the reduced detector field-of-view. The coupling of a dedicated survey telescope, the VST (Capaccioli & Schipani 2011), with a new generation wide-field optical imager, the OmegaCAM (Kuijken 2011), offers a great opportunity to investigate this issue. Similar studies for the Northern hemisphere are being carried out for the Next Generation Virgo Cluster Survey (NGVS, Ferrarese et al. 2012), and the MATLAS survey (Duc 2014).

The specific aims of the VEGAS-SSS series is to study and characterize the properties of the SSSs out to very large galactic radii, taking advantage of VEGAS imaging data. SSSs, especially the GC systems, have been studied for decades, and progress has been limited not so much by telescope collecting area but by field of view and by image quality (both to reduce contamination and to reduce the exposure times). Thus, the use of 8m and even 4m telescopes is not compelling, at least for the photometry. In this paper we show the original achievements possible with wide-field imaging from a 2.6m telescope.

So far, except for the already mentioned ongoing studies from the NGVS and MATLAS surveys, the SSSs field population of only a few galaxies has been analyzed out to large galactocentric radii (Dirsch et al. 2003; Forbes et al. 2011; Usher et al. 2012; Blom et al. 2012), though typical studies did not go much beyond $30' \times 30'$, making difficult a robust estimate of the total background contamination. Taking advantage of the large field of view of the VST we will:

- analyze the photometry in g and i bands for candidates GCs, UCDs, ECs, dSphs, etc. Furthermore, at completion VEGAS will also include r data for most of the targets, and u for selected galaxies;
- study the properties of various SSS populations as a function of galactocentric distance to limits presently unreached;
- when possible, characterize the spatial extent of sources, with the specific purpose of increasing the efficiency in distinguishing between the various classes of SSSs;
- provide catalogs of SSSs candidates essential for preparing spectroscopic follow-up campaigns based on samples suffering for low or, at least, controlled fore/background contamination. To this aim, VEGAS-SSS data covering the u bands, possibly complemented with near-IR photometry, would be particularly efficient (Muñoz et al. 2014).

Here, we present the analysis of the g and i-band of the field centered on NGC 3115, with the aim of describing the data reduction, the analysis tools and performances of the telescope, and to anticipate the future exploitation of the survey. In particular, the present work will mostly focus on the properties of the GCs system in the galaxy. Throughout the paper we verify the reliability of the methodologies used taking advantage of the large amount of literature data available for NGC 3115 (including results from HST observations and 8-10m class telescopes), and present original results on SSSs topics made possible by the use of the large-format CCD mosaic. Indeed, the case of NGC 3115, an isolated lenticular galaxy, is particularly interesting for testing the procedures used. Because of its proximity, the galaxy and its satellites were targeted by many photometric and spectroscopic studies (Hanes & Harris 1986; Capaccioli et al. 1987; Kundu & Whitmore 1998; Puzia et al. 2000, 2002; Norris et al. 2006; Arnold et al. 2011; Usher et al. 2012). Moreover, it is worth recalling that the GCs system of the galaxy is the first one beyond the Local Group with confirmed bimodal metallicity distribution, as shown by Brodie et al. (2012) from Calcium Triplet analysis, and by Cantiello et al. (2014) using optical to near-IR photometry (see also Blakeslee et al. 2010; Yoon et al. 2011).

The paper is organized as follows: the next section briefly describes the observations and data reduction procedures. We introduce the data analysis and the full catalog, providing the details of the photometric and morphological study of SSSs candidates, in Section 3. In Section 4, taking advantage of the large field-of-view of the images, we study the properties of the GC population versus galactocentric radius using a statistical background decontamination method. Section 5 is dedicated to the delicate issue of deriving SSS sizes. The final section provides a summary of our main conclusions, and describes the perspectives for the forthcoming VEGAS-SSS studies.

2. Observations and data reduction

The VST, VLT Survey Telescope, is a wide-field optical imaging telescope with a 2.6-meter aperture, operating from the u to the z with a corrected field of view of 1 degree by 1 degree. Its single focal plane instrument, OmegaCAM, is a large format (16k $\times$ 16k pixels) CCD camera with a pixel scale of $0\farcs21$ $pixel^{-1}$.

The data reduction, including dither combination, vignetting and exposure correction, astrometric solution and

Table 1. Typical properties of various classes of SSS

SSS Class	M_V (mag)	$V-I$	R_H pc	Reference
GC	-11 to $\gtrsim -5$	0.8-1.2	2-8	3, 6
EC[a]	-6 to < -4	$\sim$1.2	8-50	6, 7, 13
UCD	-14 to -9	0.7-1.3	8-100	1, 2, 4, 6
dE	-16 to -12	0.8-1.2	300-1000	5
cE	-18 to -15	~ 1.2	100-500	5, 11, 12
dSph	-12 to $\gtrsim -5$	0.8-1.2	50-1500	6, 8, 9, 10

References. (1) Drinkwater et al. (2004); (2) Mieske et al. (2006); (3) Harris (1996); (4) Mieske et al. (2012); (5)Chiboucas et al. (2011); (6) Brodie et al. (2011); (7) Madrid (2011); (8) McConnachie (2012); (9) Karachentsev et al. (2001); (10) Rejkuba et al. (2006); (11) Misgeld et al. (2009); (12) Mieske et al. (2012); (13) Huxor et al. (2005).
[(a)] Objects with similar luminosity and size have been also dubbed Faint Fuzzies (Larsen & Brodie 2000; Peng et al. 2006; Forbes et al. 2013).

Table 2. Main properties of NGC 3115

Galaxy parameters	
RA(J2000)[1]	10h05m14.0s
Dec(J2000)[1]	-07d43m07s
Galaxy Type[2]	S0
Distance adopted (Mpc)	9.4
Absolute B-band magnitude[2]	-19.9
cz[1] (km/s, Heliocentric)	663±4
Mean $E(B-V)$[3]	0.042
Effective radius R_{eff}	$57''$
Observations	
Filter (median FWHM)	Exposure time (s)
g ($\sim 0.75''$)	2695
i ($\sim 0.72''$)	1250

[1] Data retrieved from NED, nedwww.ipac.caltech.edu

[2] Hyperleda leda.univ-lyon1.fr

[3] Schlegel et al. (1998) with Schlafly & Finkbeiner (2011) recalibration

photometric calibration was performed with the VST-Tube pipeline (Grado et al. 2012). Details about the overall data quality can be found in Capaccioli et al. (2014). In particular the FWHM of the PSF varies for $< 0''.05$ across the field of view, and the internal astrometric accuracy is $\sim 0''.035$ (the *rms* with respect to the USNO-B1 catalog is $\sim 0''.2$).

In order to improve the analysis of the spatial extent of the sources in the frame, we restricted our analysis to the imaging data with average PSF FWHM$\leq 0''.8$. With this choice the exposure time is reduced by $\sim$30% in g and $\sim$ 50% in i with respect to the total integration time available.

Basic properties for the target and the optical observations are listed in Table 2. The g-band image of NGC 3115 is shown in Figure 1.

Given our purpose of studying SSSs, we need to minimize the contamination due to the presence of the light from NGC 3115. To model and subtract the galaxy, we used the ISOPHOTE/ELLIPSE task in IRAF/STSDAS (Jedrzejewski 1987)[1]. The modeling failed to match the central thick disk region, which implied poor detection of the sources within the inner $\sim 2'$ area[2]. However, the central regions of the galaxy have been accurately inspected using a $\sim 10' \times 7'$ mosaic obtained with the ACS camera on board of the *Hubble Space Telescope* (HST; Jennings et al. 2014). The ACS study relies on data with similar wavelength coverage and g-band depth with respect to the ones used here. Given the higher resolution of HST data, we do not make any attempt to recover the sources in the central $\sim 3.5' \times 1.5'$ poorly modeled regions along the galaxy major axis.

3. Photometry and size estimates

To produce a complete catalog of all sources present in the VST field of view, we run SExtractor (Bertin & Arnouts 1996) on the galaxy-model subtracted frame, independently for each filter.

We obtained aperture magnitudes within a 6 pixel diameter aperture ($\sim 1''.26$ at OmegaCAM resolution), and applied aperture correction to infinite radius. The aperture correction, derived from the analysis of the curve of growth of bright isolated point-like sources (see Cantiello et al. 2005, 2011, for more details), is 0.52 ± 0.01 and 0.46 ± 0.01 mag in g and i, respectively. For extended sources, i.e. sources spatially more extended than the instrumental FWHM of the PSF (see below), we used the SExtractor Kron-like elliptical aperture magnitude. Finally, the photometric catalogs in the two bands were matched adopting $0''.5$ matching radius. The final photometric catalog contained $\sim$47000 sources.

Due to the large areal coverage, there is a non-negligible variation of Galactic extinction from one side to the other of the field ($\Delta A_g \sim 0.07$ mag). We obtained the local extinctions from the dust maps by Schlegel et al. (1998) and used the reddening factors from Schlafly & Finkbeiner (2011). The final extinction map is shown in Figure 2. All further colours and magnitudes in the paper are corrected for extinction unless otherwise stated. Other details on the photometric properties of the images analyzed (completeness an limiting magnitudes) are given in Appendix A.

The colour magnitude diagram of the full sample of g and i matched sources is shown in Figure 3 (panel (a)).

It is very important to emphasize that the selection of SSSs based on one single colour, the $(g-i)$, is inherently uncertain, resulting in a catalog with large fractions of contaminating sources (foreground stars and background galaxies, Durrell et al. 2014). The selection with a further optical color would certainly reduce the fraction of contaminants, especially if u band photometry is available. However, a contaminant-free catalog based on optical photometry is basically unattainable. It is useful to highlight, though, that the coupling of optical data with just one near-IR band is very effective in reducing the fraction of

[1] IRAF is distributed by the National Optical Astronomy Observatory, which is operated by the Association of Universities for Research in Astronomy (AURA) under cooperative agreement with the National Science Foundation.

[2] A test with GALFIT (Peng et al. 2002), a further program designed for modeling two-dimensional brightness profiles, also failed the modeling of the central galaxy regions. We also obtained a galaxy-subtracted frame as described in Jordán et al. (2007) and Cantiello et al. (2014, which modeled NGC 3115 from near-IR data). Such method uses the SExtractor spline background derived from the image logarithm, and provided very flat residuals. However, the latter procedure affects badly the shape of slightly extended objects, thus it is not suitable for the purposes of the present study.

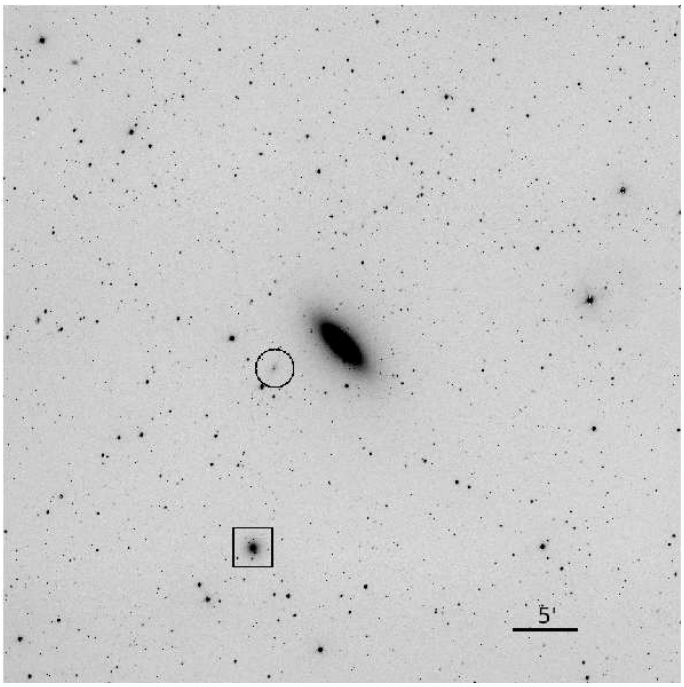

Fig. 1. VST/OmegaCAM g-band image of NGC 3115. North is up, East is left. The image size is $52.5' \times 52.5'$. The black square and circle mark the position of NGC 3115B and KK 084, respectively.

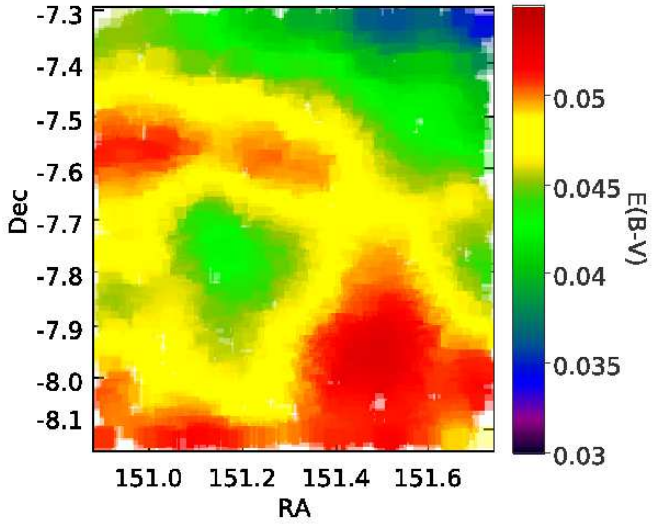

Fig. 2. Extinction map over the area analyzed. The colorbar shows the extinction to color mapping.

contamination to the GC and UCD catalogs to less than $\sim 5\%$ (Muñoz et al. 2014).

To partly overcome the problem of selecting SSSs relying on only one optical colour, one can use statistical decontamination techniques (see Section 4), and/or add a further selection criterion: the physical extent of the source (Table 1). The methodology that we will adopt to derive objects sizes is described below, while the effectiveness and the practical issues in using object sizes as a selection parameter will be discussed in Section 5.

3.1. Size and shape measurements as compactness criterion

As shown in Table 1, if one can estimate the half-light radius R_h of SSSs then the objects shape can be used together with photometric properties to classify the system. However, size measurements can be very challenging, especially with ground-based imaging data. Furthermore, in general one can only measure angular sizes which, to be transformed in linear scale, require the previous knowledge of the object distance. In spite of this, angular sizes and shapes have been estimated for a large sample of SSSs in different environments and with various ground- and space-based telescopes (e.g. Larsen 1999; Larsen & Brodie 2003; Jordán 2004; Cantiello et al. 2007; Caso et al. 2013; Puzia et al.

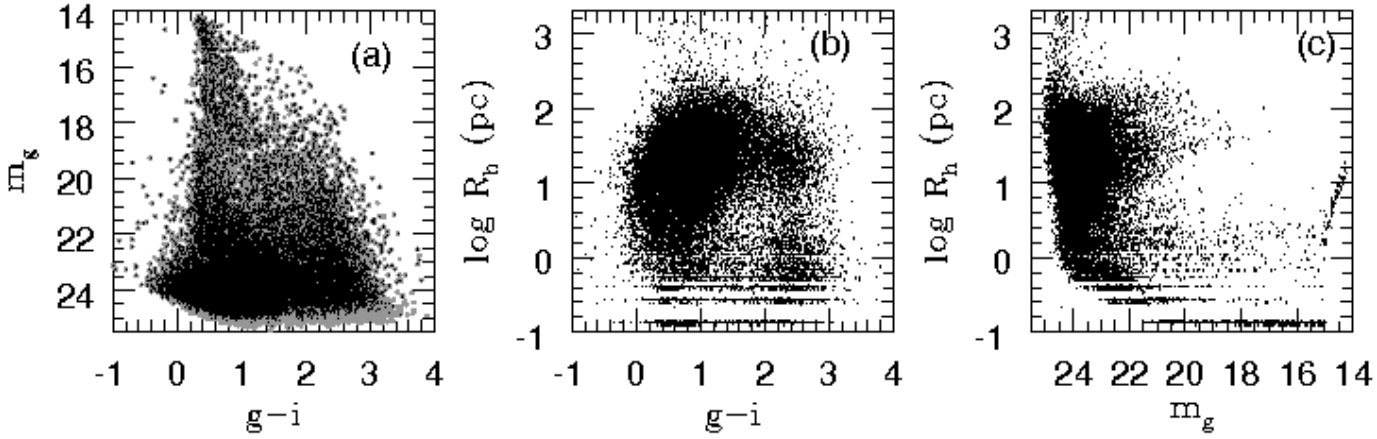

Fig. 3. Photometry and sizes of SSS candidates in NGC 3115. Panel (*a*): colour magnitude diagram for the full sample of g and i matched sources (gray dots), and for the sources with size estimates (black points). Panel (*b*): apparent size versus colour diagram. Panel (*c*): apparent size versus magnitude diagram.

2014). In what follows we describe how object sizes have been estimated for objects in the VEGAS-SSS fields.

Given the difficulty posed by the task, to estimate the intrinsic size of a source exceeding some instrumental-dependent size limit, specific tools have been designed and implemented to analyze the light profiles of sources with intrinsic sizes comparable or slightly smaller than the instrumental PSF. For VEGAS-SSS we choose to adopt Ishape[3] to obtain structural parameters (in particular R_h and the axis ratio b/a) of SSSs. Ishape is optimized for modeling the light distribution for marginally resolved sources down to 1/10 of the FWHM of the PSF (Larsen 1999; Larsen & Richtler 2000). In such context, NGC 3115 is one of the most attractive targets in the survey, being also one of the nearest. At the adopted distance of 9.4 Mpc (Tonry et al. 2001, using the updated calibration zeropoint from Cantiello et al., 2013), and given the FWHM of the images (Table 2), Ishape can be used to determine the physical extent of objects with $R_h \geq 3.5$ pc. For the reasons explained in Section 5, we will take into account also objects down to $R_h \sim 2$ pc. The measurement of source size below the FWHM is particularly demanding in terms of signal-to-noise ratio, SNR, for this reason we have checked that the i-band data currently on hand did not provide us of an adequate SNR, hence in the following we will use the R_h estimates derived from the g-band only.

Ishape reaches a convergence for $\sim$ 30000 of the input $\sim$ 47000 sources in the photometric catalog. The size-colour and size-magnitude plots for the sample of sources for which we have structural parameters are shown in Figure 3 (panels (*b*) and (*c*), respectively).

More details on Ishape runs are given in Appendix B.

3.2. Final catalog

The final catalog resulting from the colour and size/shape criteria is given in Table 3. The catalog contains the full list of $\sim$ 47000 sources matched in the g and i catalogs. For each source, the following parameters are reported: (1) VEGAS-SSS ID, (2) and (3) right ascension and declination (J2000), (4) galactocentric distance, (5) g magnitude and error, (6) SExtractor CLASS_STAR parameter in the g band CS_g, (7) i magnitude and error, (8) SExtractor CLASS_STAR parameter in the i band CS_i; (9) $(g-i)$ color; (10) local reddening; (11) signal-to-noise ratio from Ishape; (12) FWHM of the source; (13) effective radius; (14) object minor to major axis ratio (b/a); (15) notes. The absolute value of R_h in pc depends on the distance adopted, thus it is wrong for all unknown contaminating fore/background sources. In Section 5 we will discuss the percentage of contamination expected on the basis of comparison with data from the literature.

4. GC population properties as a function of galactocentric distance: statistical decontamination of the sample

In this section, we analyze the colour and magnitude distribution of SSSs in the field of NGC 3115. In particular, because they dominate the SSS population in the galaxy core, we focus on GCs, making use of statistical decontamination of background sources. To have a better statistics for the background subtraction, we use the entire VEGAS-SSS catalog of g and i matched sources ($\sim$ 47000 objects), and select as good GCs candidates sources: *a*) in the colour range for $0.4 \leq (g-i) \leq 1.25$ mag (e.g. Faifer et al. 2011; Kartha et al. 2013; Vanderbeke et al. 2014); *b*) maximum photometric error $\Delta(g-i) = 0.15$ mag for colour analysis ($\Delta m_g = 0.5$ mag for magnitude analysis); *c*) SExtractor star-galaxy $\langle CS \rangle \geq 0.2$, to avoid contamination from sources that are trivially background galaxies; *d*) and $m_g \geq 18$ mag, i.e. sources $\sim 4\ \sigma_{TOM}$ brighter than m_g^{TOM} are not taken into account (see below). Thus, for the analysis presented in this section we do not apply any restriction on R_h.

[3] The software can be downloaded at http://baolab.astroduo.org/. For the present work we used the release 0.94.1d.

Table 3. Photometry and size estimates for the matched gi catalogs. The full table is available in the electronic version of the journal.

	Position			Photometry						lshape results				
ID	RA (J2000)	Dec (J2000)	R_{gal} ($'$)	m_g (mag)	CS_g	m_i (mag)	CS_i	$(g-i)$	$E(B-V)$	SNR	FWHM ($''$)	R_h (pc)	b/a	Note[a]
(1)	(2)	(3)	(4)	(5)	(6)	(7)	(8)	(9)	(10)	(11)	(12))	(13)	(14)	(15)
4	151.040149	-8.155928	30.7	25.35± 0.20	0.45	24.10± 0.23	0.56	1.250	0.053	...	...	...	...	0
6	151.484945	-8.155959	28.3	24.51± 0.09	0.70	23.91± 0.19	0.72	0.602	0.052	...	...	...	...	0
92	151.348259	-8.155089	26.3	23.97± 0.10	0.02	21.86± 0.08	0.06	2.109	0.051	18.6	$0.95^{0.33}_{-0.95}$	12.5	0.85	0
93	151.091210	-8.154886	29.2	24.26± 0.12	0.39	23.05± 0.14	0.38	1.210	0.053	11.4	$1.14^{0.11}_{-1.14}$	15.0	0.86	0
293	151.571415	-8.153376	30.4	21.78± 0.02	0.03	21.27± 0.04	0.03	0.502	0.051	106.7	$2.49^{0.03}_{-0.09}$	34.8	0.97	1
993	151.117979	-8.143415	27.9	21.86± 0.02	0.03	21.19± 0.04	0.04	0.675	0.053	94.8	$1.74^{0.02}_{-0.10}$	22.0	0.78	1
1396	150.878854	-8.138160	35.8	22.37± 0.02	0.86	21.67± 0.03	0.26	0.700	0.052	64.3	$0.53^{0.08}_{-0.01}$	6.7	0.77	2

[(a)] 0: source common to both g and i cataloges without lshape data, or rejected from the *reference* and *best* samples; 1: source in the *reference* sample; 2: source in the *best sample*.

4.1. Background determination

Our approach relies on the assumption that all sources beyond some limiting galactocentric radius, R_{bg}, are foreground or background contaminants, with a uniform spatial distribution over the field. In particular, we adopted $R_{bg} = 23'$ (see also Section 5), corresponding to ~ 65 kpc at the distance of the galaxy. Taking as reference the GCs systems in the Milky Way and M 31, we estimate that a fraction of $\sim 2-3\%$ GCs brighter than $m_g \sim 25$ mag (the approximate 90% limiting magnitude in g, see Figure 3, and Appendix A) might still be in the background sample because of their large galactocentric distances $R_{gal} \gtrsim 65$ kpc. More in detail, the Galaxy has seven GCs, over 157, at $R_{gal} \gtrsim 65$ kpc (Harris 1996, 2010 release), only three of them are brighter than the detection limit of our photometric catalog. This implies that, if placed at the distance of NGC 3115, and for random viewing angles, $\lesssim 2\%$ of the MW GCs would be included in the background sample. The GCs catalog of M 31 by Galleti et al. (2004, RBCv5), selected using optical to near-IR colour cuts (Muñoz et al. 2014), contains 447 GC candidates none of which at galactocentric distance larger than 35 kpc. On the other hand, Huxor et al. (2014), using the CFHT/MegaCam data of the PAndAS survey, discovered 59 new GCs at large galactocentric distances in Andromeda: 19 of them would be brighter than our magnitude cut, and with a projected distance larger than 65 kpc from the galaxy center. This corresponds to a fraction $\sim 3\%$ the total, assuming a total population of at least 700 GCs (638 from RBCv5, 59 from PAndAS).

Adopting $R_{bg} = 23'$ means that $\sim 40\%$ of the image is used for the analysis of contamination. The possible future addition of further bands will allow to increase the inner radius for the selection of GCs (more in general, of SSS satellites), allowing to use a smaller fraction of the detector to characterize the contamination.

Under such assumption, the difference between the surface density at galactocentric distance $R_{gal} \leq R_{bg}$ and $R_{gal} > R_{bg}$ gives the residual density of sources in NGC 3115, mainly GCs.

We proceeded as follows. We first estimated the surface density of background objects per square arcminute at given colour (or magnitude), Σ_{bg}, adopting the selection criteria $(a)-(d)$ given above, plus the galactocentric distance. Then, the total surface density of objects within elliptical concentric regions, $\Sigma(R_{gal} \leq R_{bg})$, is estimated using the same criteria on colour (or magnitude), adopting different inner radii, starting from $R_{gal} = 2'$ out to $R_{gal} = R_{bg}$, with $1'$ steps. The geometry of the ellipses, with constant ellipticity $\epsilon = 0.5$ and position angle $PA = 45°$, is assumed according to the results of Capaccioli et al. (2014) (see also Arnold et al. 2011; Jennings et al. 2014). In the following, R_{gal} is the semi-major axis, if not stated otherwise.

The overdensity of sources at given colors (or magnitude) associated with NGC 3115 is finally estimated as the difference $\Sigma_{Host} \equiv \Sigma(R_{gal} \leq R_{bg}) - \Sigma_{bg}$.

4.2. Colour Distribution

The panels in Figure 4 show the density histograms $\Sigma(R_{gal} \leq R_{bg})$, Σ_{bg}, and Σ_{Host} versus colour (from left to right, respectively). In each panel, darker colour refers to regions with smaller inner radii. The histograms after the first innermost radius have been smoothed for sake of clarity. In the first panel of the figure, the density distribution shows the presence of a dip at $(g-i) \sim 0.9$ mag, and two well defined peaks at $(g-i) \sim 0.75$ and 1.00 mag whose prominence decreases, but does not go to zero, as larger radii are considered.

For background sources (Figure 4, Σ_{bg} middle panel) the density distribution does not show relevant features, and appears nearly flat over the colour interval shown. As expected, the colour distribution of the difference diagram (Figure 4, Σ_{Host} right panel) shows two distinct color peaks at all radii.

To investigate the properties of the colour distributions in panel (c) at each given radius, we used the "Gaussian mixture modeling" code (GMM, Muratov & Gnedin 2010)[4]. More in details, we randomly populated the difference distribution, Σ_{Host}, with a fixed number of sources ($N_{sim} \sim 1500$), and then run the GMM code on the repopulated sample.

The results of the GMM run are given in Table 4, where for each R_{gal} it is reported the position of the peak and width of the blue and red distributions, as well as the fraction of GCs associated with each populations (in parentheses). The total fraction, in some cases, does not equal one, because of the presence of a minor very red peak. Figure 5 shows the positions of the blue and red peaks, the standard

[4] GMM uses the likelihood-ratio test to compare the goodness of fit for double-Gaussians versus a single-Gaussian. For the best-fit double model, it estimates the means and widths of the two components, their separation DD in terms of combined widths, and the kurtosis of the overall distribution. It also provides uncertainties based on bootstrap resampling. In addition, the GMM analysis provides the positions, the relative widths, and the fraction of objects associated with each peak.

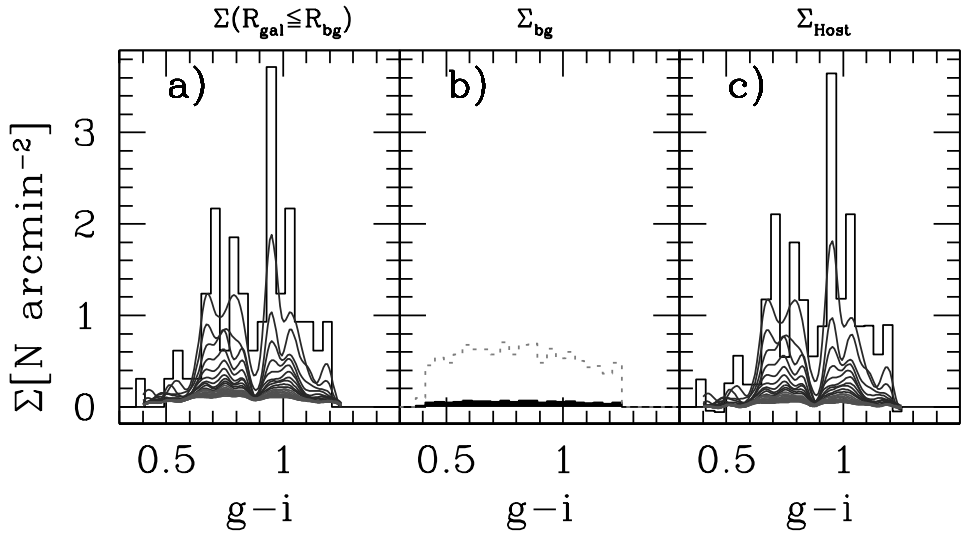

Fig. 4. Surface density histograms versus color. Panel (a): Surface density for sources within $R_{gal} \leq R_{bg}$. Darker colour refers to areas with smaller galactocentric radii. Panel (b): same as left, but for background sources at $R_{gal} > R_{bg}$. For sake of clarity dotted histogram shows the density histogram times a factor 10. Panel (c): residual surface density, $\Sigma(R_{gal} \leq R_{bg}) - \Sigma_{bg}$.

Table 4. Results of GMM at various galactocentric radii.

$R_{gal}(')$	$(g-i)_0^{blue}$	$(g-i)_0^{red}$	N_{GC}^{sel}
2.0	0.79 ± 0.18 (0.64)	1.01 ± 0.07 (0.30)	68
3.0	0.78 ± 0.15 (0.69)	1.00 ± 0.06 (0.26)	150
4.0	0.75 ± 0.14 (0.64)	1.02 ± 0.07 (0.30)	204
5.0	0.76 ± 0.14 (0.74)	1.01 ± 0.05 (0.19)	268
6.0	0.76 ± 0.14 (0.70)	1.01 ± 0.05 (0.23)	315
7.0	0.76 ± 0.14 (0.70)	1.02 ± 0.06 (0.25)	364
8.0	0.76 ± 0.13 (0.65)	1.02 ± 0.06 (0.29)	400
9.0	0.75 ± 0.13 (0.65)	1.01 ± 0.06 (0.29)	454
10.0	0.75 ± 0.13 (0.65)	1.00 ± 0.05 (0.23)	518
11.0	0.76 ± 0.13 (0.66)	1.00 ± 0.06 (0.24)	562
12.0	0.75 ± 0.13 (0.67)	1.00 ± 0.06 (0.27)	612
13.0	0.75 ± 0.13 (0.69)	1.00 ± 0.05 (0.22)	661
14.0	0.75 ± 0.14 (0.69)	1.00 ± 0.05 (0.21)	718
15.0	0.75 ± 0.13 (0.70)	1.00 ± 0.05 (0.23)	768
16.0	0.74 ± 0.14 (0.69)	1.01 ± 0.08 (0.29)	833
17.0	0.75 ± 0.14 (0.70)	1.02 ± 0.07 (0.28)	890
18.0	0.75 ± 0.13 (0.69)	1.00 ± 0.05 (0.23)	963
19.0	0.75 ± 0.13 (0.69)	1.00 ± 0.05 (0.22)	1024
20.0	0.75 ± 0.13 (0.69)	1.01 ± 0.06 (0.24)	1086
21.0	0.75 ± 0.14 (0.70)	1.00 ± 0.05 (0.22)	1159
22.0	0.73 ± 0.14 (0.66)	1.01 ± 0.08 (0.31)	1247

deviation of each distribution, and the fraction of objects associated with each peak (given by symbol size).

In the table we also report the number of GC candidates selected according to the $(a) - (d)$ selection criteria given above (N_{GC}^{sel}, column). Using the average surface density of contaminants $\Sigma_{bg} = 0.056 \pm 0.014$ $[N/arcmin^2]$, and the N_{GC}^{sel} listed, one can easily derive the expected number of GCs corrected for contamination at each elliptical radius. As an example, the area with $R_{gal} \sim 6 - 8'$ roughly corresponds to the ACS area inspected by Jennings et al. (2014), and is expected to contain $\sim 310 - 390$ GCs, to be compared with the 360 candidates found with ACS.

We note that the position of the two peaks and their width are consistent at all radii inspected, and agree very well with the recent similar analysis on the same host galaxy (Faifer et al. 2011; Usher et al. 2012). A closer inspection to the data in Figure 5, and Table 4 reveals the presence of important features. First, a colour-R_{gal} correlation is observed for the blue GC component (Pearson correlation coefficients $r_{xy} \sim -0.8$), with a ~ 0.06 mag colour difference between the inner and outer region. There is no, or a very weak, colour-radius correlation for the red GCs ($r_{xy} \sim -0.25$). Furthermore, the fraction of sources in the red sub-population shows a slight but significant decrease with respect to the blue one at large radii. The width of both sequences is relatively stable with radius, with the blue distribution being broader at all radii.

These properties support a scenario where blue GCs are associated with the galaxy halo, while red ones are more centrally concentrated and associated with the bulge stellar component in the galaxy (Kissler-Patig 1997; Côté et al. 1998; Forte et al. 2005; Liu et al. 2011).

In order to study the population of GCs associated with NGC 3115 excluding the GC contaminants from the neighboring fainter galaxies, we also carried out several tests rejecting all GC candidates within 2-3′ from KK 084 and NGC 3115B. The first galaxy, KK 084, is a dSph with center at $R_{gal} \sim 5.5'$ from NGC 3115, and a non-negligible population of GC candidates, having a specific frequency $S_N \equiv N_{GC}\ 10^{0.4(M_V+15)} = 10$ (Harris & van den Bergh 1981; Puzia & Sharina 2008). In spite of the relatively large S_N, the net effect on the properties of the GC system in NGC 3115 is negligible. None of the sources in NGC 3115B falls in the elliptical shaped area of NGC 3115 inspected here.

In Figure 5 we added the data from Arnold et al. (2011), which are part of the SLUGGS survey (Brodie et al. 2014). Gray circles in the figure mark spectroscopic confirmed GCs, green dots mark the running mean for gray dots. We find very good matching between the mean VEGAS-SSS colour obtained with the statistical decontamination approach presented in this section, and the colour of the spectroscopically confirmed GCs.

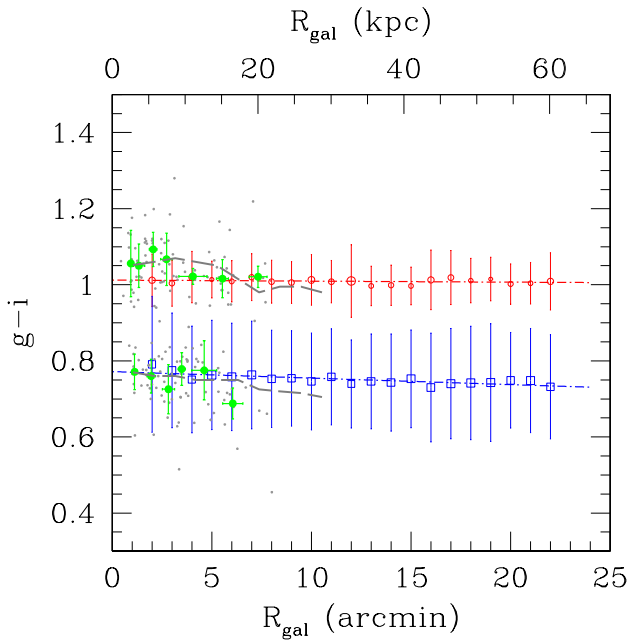

Fig. 5. Position and width of the blue and red GCs (blue squares and red empty circles, respectively) at different R_{gal} as obtained from GMM. Symbol size is proportional to the fraction of objects associated with each peak. A fit to the data is shown with dot-dashed lines for both subpopulations. Gray dots show spectroscopic confirmed GCs from Arnold et al. (2011). Full green points mark the running mean (median from equal number of data) of gray points. Gray long-dashed lines mark the rolling fits of the blue and red GC peaks as derived by Arnold et al. (2011) obtained from a combination of spectroscopic and photometric selected GCs.

Arnold et al. (2011) also derived the radial profiles out to $R_{gal} \sim 10'$ combining the spectroscopic sample with a photometric sample, corrected for contamination using *"an iterative Monte Carlo scheme"* (gray lines in Fig. 5). The matching of the VEGAS-SSS and SLUGGS colour profiles for blue GCs is good at all common radii.

We note that at $R_{gal} \geq 6'$ the colour profiles from Arnold et al. depend mostly on the properties of the photometric sample, thus the transition appearing in both the blue and red GCs profiles at $6 \geq R_{gal} \geq 8'$ is strongly weighted toward the photometric sample.

For the blue GCs, the difference between the mean from VST and Arnold et al.'s colour of spectroscopically confirmed GCs at $R_{gal} \leq 6'$ is Δ(g-i) $^{blue} < 0.01$ mag. For the red GCs component the difference is Δ(g-i) $^{red} \sim 0.03$ mag.

By coupling the spectroscopic and photometric samples (gray dashed line), Arnold et al. found that the red GCs are on average bluer at larger galactocentric distances as for blue GCs. The presence of a radial trend in the red GCs from SLUGGS data appears mostly beyond $R_{gal} \sim 6'$, where the photometric sample dominates over the spectroscopic one. Furthermore, the red GCs profile is nearly flat for $R_{gal} \leq 5.5'$ and $R_{gal} \geq 7.5'$, with a ~ 0.07 mag colour transition in between.

Overall, the radial colour profiles of GCs from the VEGAS-SSS and SLUGGS are consistent if one takes into account the error envelopes, the intrinsic width of the distribution at fixed R_{gal} and the different analysis approaches adopted.

The good matching appears even more strikingly if one takes into account that the data from Arnold et al. (2011), are obtained by coupling *gri* band imaging data from Suprime-Cam at the 8.2m Subaru telescope, and spectroscopy from the 10m Keck-II telescope with DEIMOS.

In conclusion, the comparison shown in Figure 5 provides a strong evidence in support of the efficiency of the approach adopted here to analyze the properties of the GC system out to more than ~ 20 galaxy effective radii. It also shows that original results are obtained, even with the photometry in only two passbands, when using the wide-field imaging data from the 2.6m VST telescope.

4.3. Surface density profiles

The radial profiles of the projected surface density for GC candidates are shown in Figure 6. The surface density at each radius is obtained as the difference between the total density of sources with $R_{gal} \leq R_{bg}$, and the background density.

Taking advantage of the results obtained with GMM on the blue/red GCs, we also analyzed the radial density profiles of the blue/red subpopulations. Dividing the GCs into subpopulations, adopting a sharp blue/red separation at $g-i = 0.9$, the radial profile for the red GCs appears steeper than that for the blue GCs. Moreover, both density profiles follow very closely a $r^{1/4}$ de Vaucouleurs profile (dotted lines), and both are shallower than the galaxy light profile, showing a behavior similar to other galaxies (e.g. NGC 4636 and NGC 3923, Dirsch et al. 2005; Norris et al. 2012).

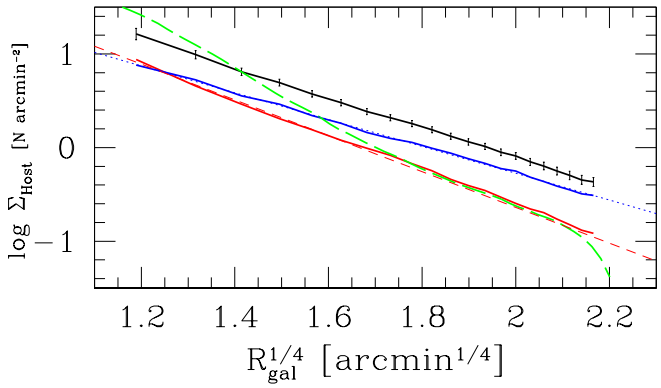

Fig. 6. Surface density profiles of blue, red, and total GC population (blue, red and black lines, respectively). The galaxy surface brightness profile in *g* band from Capaccioli et al. (2014) is also reported with green long-dashed line. The linear fit to the surface density is shown with dotted lines (blue-dotted, red-dashed for the blue/red GCs, respectively). The scale of the galaxy profile is arbitrary.

The steeper starlight gradient, compared with GCs density (blue or total GC density), suggests that the GC system of NGC 3115 extends farther than the surface brightness profile of the galaxy halo. This result is consistent with the general picture of the GC system being spatially more extended than the host galaxy (Harris 1991; Harris et al. 2000; Forbes et al. 2006; Alamo-Martínez et al. 2012; Kartha et al. 2013).

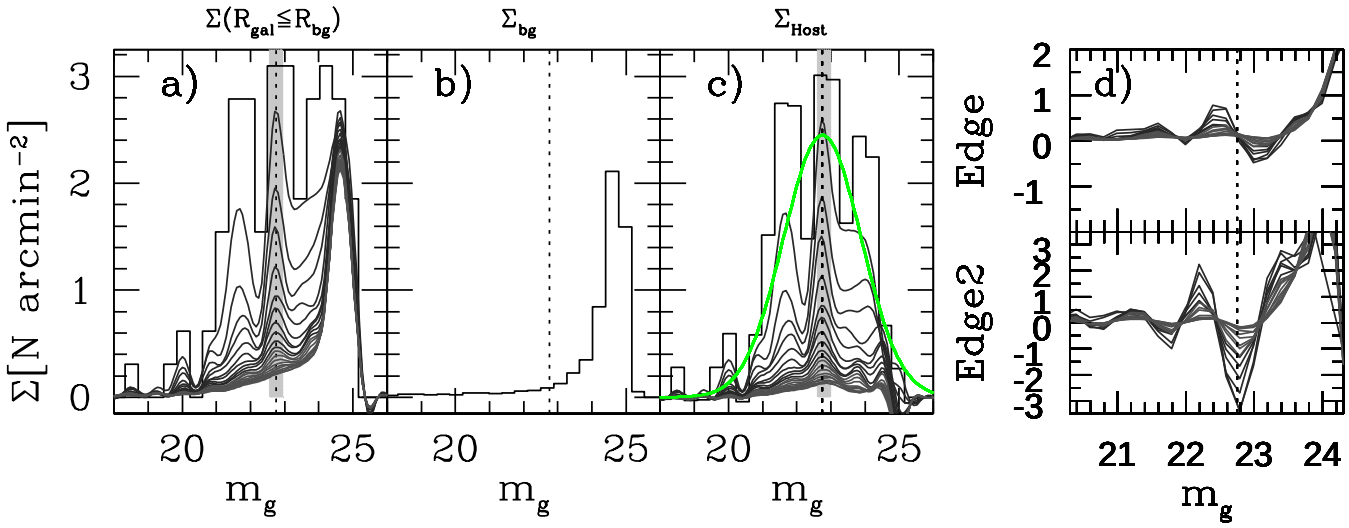

Fig. 7. Surface density histograms versus magnitude. Panels (a) to (c): as in Figure 4 but magnitude is used instead of colour. The vertical dotted line shows the position of the TOM. The ~ 0.2 mag tolerance for the peak position (gray shaded area) is also shown as well as the best fit Gaussian to the GCLF (green line; $m_g^{TOM} = 22.75$ mag, $\sigma_{TOM} = 1.14$). Panel (d): edge and second-run edge (Edge2) functions.

A further feature in Figure 6 is the matching of the density profile for red GCs with the galaxy light profile at $R_{gal} \geq 7.5'$ ($R_{gal}^{1/4} \geq 1.65$), while the surface density of GCs at smaller radii is slightly lower. Such depletion has already been observed in galaxies brighter than NGC 3115 (e.g. Dirsch et al. 2005; Goudfrooij et al. 2007), and associated with higher efficiency of GC-disruption mechanisms in the inner galaxy regions (dynamical friction, two-body relaxation and GC tidal shocking, Vesperini 2001; Goudfrooij et al. 2007), suggesting that the galaxy has undergone a relatively quiescent evolution, without major star-forming events, which would have increased the inner density of red GCs.

4.4. Luminosity Function: GCLF

Adopting the same approach used for colors in Section 4.2, we analyzed the luminosity function of sources in the field, with the specific purpose of inspecting the GC luminosity function (GCLF) to independently estimate the galaxy distance modulus (Harris 2001), and further derive the position of the turnover magnitude m_g^{TOM} as a function of galactocentric distance.

Figure 7 shows the surface density distribution obtained as described in previous section, with the difference that in this case we used the total g magnitude, instead of $(g-i)$ colour. The GCLFs derived are corrected for radial-dependent completeness as described in Appendix A. Panel (a) in the figure shows the presence of various local maxima in the density distribution, whereas the distribution of background sources, in panel (b), has a power law increase with a drop between $m_g \sim 24$ and 25.5 mag, due to the completeness limit given by the adopted selection criteria. The density distribution of sources in the host galaxy, shown in panel (c), reveals the presence of a major peak at $m_g \sim 22.75$ mag.

To inspect the presence of a discontinuity in the luminosity function due to the TOM, we adopt a quantitative method introduced by Lee (1993) to identify the position of the RGB Tip in Galactic resolved GCs. The results of such edge-detection method (based on the Sobel filter, see Appendix A) are shown in panel (d) of Figure 7. Although the uncertainties in the surface density, and their propagation in the definition in the edge and second-edge functions are certainly large, the diagrams highlight the presence of an inflection point (edge) and a maximum (edge2) around $m_g \sim 22.75$ mag as expected at the TOM (see Figure A.2[5]).

In Figure 7, we also show the gaussian GCLF with arbitrary peak normalization, assuming turnover TOM magnitude $m_g^{TOM} \sim 22.75$, with $\sigma_{TOM} = 1.14$ derived from Jordán et al. (2009, eq. 18). A ~ 0.2 mag tolerance area around m_g^{TOM} is also shown. Adopting the absolute value for the turnover magnitude from the ACS Virgo Cluster Survey for galaxies with $M_B < -18$, $M_g^{TOM} = -7.2 \pm 0.2$ mag, we estimate a distance modulus $\mu_0 = 29.95 \pm 0.3$, in good agreement with the literature distance of the galaxy (Table 2).

Furthermore, thanks again to the large area inspected, we also probe the variation of m_g^{TOM} to large projected galactocentric radii. The data in Figure 7 (panel c) reveal a TOM essentially constant over the spatial scales inspected, as also found in other galaxies (Jordán et al. 2007).

On the basis of the results shown in Figure 7 and in Figure 4, we deduce a low contamination rate in the regions within $R_{gal} \leq 8'$ (first six darker curves in the figures), as the luminosity and colour surface density of contaminants, Σ_{bg} shown in the central panels, can be one order of magnitude smaller than density in the inner regions. This implies

[5] Inspecting the edge functions two other possible TOM-point candidates are located at $m_g \sim 22.2$ and 23.2 mag (see Appendix A). However, both magnitude values are ruled out as TOM peak by the shape of the GCLF.

that the rate of contamination of the VEGAS-SSS catalog for NGC 3115 is quite low for the innermost $\sim 8'$. As an example, the background density at $m_g \sim 23$ mag is $\Sigma_{bg} \sim 0.3[N/arcmin^2]$, while the density of sources within $R_{gal} \leq 8'$ is ~ 3.5 times larger, and gets ~ 7 times larger at $R_{gal} \leq 4'$.

We further inspected how the TOM differs between red and blue GCs, a test that is not often possible and here feasible thanks to the large area inspected. After dividing the blue/red GCs adopting a sharp colour separation at $(g-i)$ =0.9, we carried out the analysis described above on the luminosity functions blue and red GCs. The results are shown in Figure 8, where the total luminosity function $\Sigma(R_{gal} \leq R_{bg})$, the background corrected ones Σ_{Host}, and the Edge/Edge2 diagrams are shown for the blue and red GCs (upper and lower panels, respectively). Despite the samples adopted are numerically smaller than before, the corrected GCLF still shows the presence of a peak around the same m_g^{TOM} of the total GC population. By estimating the position of the TOM with the Edge functions (right panels in the figure), the interesting point here is that there appear to be a $\sim$ 0.2 mag offset between the TOM of red and blue GCs, with the red system being fainter. From the point of view of stellar population models, if the GCs mass function is universal across metallicity, the Gaussian mean of the blue GCs is expected to be brighter than that of the red one (Ashman et al. 1995; Di Criscienzo et al. 2006; Jordán et al. 2007). Observationally, our result confirms previous evidences obtained from data with much smaller surface coverage (Whitmore et al. 1995; Puzia et al. 1999; Peng et al. 2009). Further improvements on this will be allowed by the analysis of new galaxies in the VEGAS-SSS sample, with the possible inclusion of u and r band data in the SSSs selection process.

As a final comment, we highlight that the depth, in terms of absolute magnitude, and the image quality for the other galaxies in the VEGAS sample will be similar to the one inspected here, thus we expect that using the tools presented here[6], we will reliably analyze the colour distributions and study GCs luminosity function for all other targeted galaxies out to unreached galaxy effective radii. Moreover, for objects at larger distances the background decontamination methods described in this section will likely be more effective because of the larger galactocentric distances inspected.

5. Object sizes: comparison with literature and analysis

In this section we present a detailed analysis of the properties of the SSS in the field of NGC 3115, and concentrate on the sample of objects with R_h estimates from Ishape.

5.1. Comparing VEGAS-SSS and HST/ACS derived photometry and sizes

As already mentioned, using the photometry and size measurement tools described in the Section §3.1, we ended up with a catalog containing ∼30000 sources. We compared our measurements with the estimates by Jennings et al. (2014), based on ACS/HST g_{F475W} and z_{F850LP} observations. At the distance of the galaxy, all sources in the field of NGC 3115 with $R_h \geq 1$ pc appear resolved at the pixel resolution of the ACS. Thus we assume the R_h measured from ACS data as best representing the true distribution of R_h for the GCs in the galaxy, within the limited common area.

The matching of the GCs list from Jennings et al. (2014) with the VST catalog (using 0.″5 radius) contains a list of $\sim$ 270 of the 360 candidates[7]. Nearly $\sim$ 70% of the unmatched sources are GCs located in the central galaxy regions, where we do not model and subtract the galaxy light profile. The remaining $\sim$ 30% of missing objects are faint sources, undetected in the shallower i image, or objects blended with bright neighbors. The number of missed sources beyond the central regions drops to ~ 10 if the sole g band catalog is considered (again faint or blended sources). The comparisons of g-band ACS and VEGAS-SSS photometry, shown in Figure 9 versus magnitude and colour, reveals very good agreement. In the figure, the full ACS catalog (Z. Jennings, private communication) and the sole GCs sample are considered separately. For sake of homogeneity the comparison with ACS is done using constant extinction. The large scatter for the full sample (left panels) is due to the presence of extended background sources, whose aperture magnitude does not represent a good estimate for the total magnitude, neither for ACS nor for VEGAS-SSS. Comparison of photometry for the sole GCs (right panels in the figure) indicates negligible mean residual difference, both in magnitude and colour.

We also compared the R_h estimates from VEGAS-SSS with the ACS ones. In the comparison one must note that the list of SSS candidates is not contaminant free in either catalogs, as it includes background sources whose (linear) R_h estimates are wrong because they are derived according to the distance of the galaxy. In spite of this, the ACS VEGAS-SSS comparison is still valid since the same distance modulus is assumed in both analysis. Moreover, it should also be noted that the size estimates are not equally good for the full sample of objects measured. Thus, we define a *reference* sample of VEGAS-SSS candidates with reliable structural and photometric parameters, adopting the following criteria derived on the basis of the comparison with ACS photometry and objects shape:

- Ishape signal-to-noise ratio SNR$\geq$ 30 (Larsen 1999);
- total relative error on R_h $\leq$30%;
- for each source where the iteration to derive R_h was successful, Ishape provides a cutout of the image with the object analyzed, the model brightness profile, the residuals between them, and the weighting map (Larsen 1999). To reject sources with large residuals (see Appendix C, Figure C.4), but otherwise good SNR and FWHM error, after various experiments where we inspected the statistical properties of the residual cutouts, we chose a limit of $median/rms \leq 0.3$ for good candidates. This criterion applies for objects with contaminating neighbors or structures not accounted for by the previous criteria;
- as in Section §4 we adopted colour range $0.4 \leq (g-i) \leq 1.25$ mag both for GCs and UCDs;
- maximum photometric uncertainty $\Delta m_g = 0.15$ mag;

[6] Apart from the size/shape inspection, that will hardly be possible for GCs in distant galaxies, but doable for the UCDs.

[7] We found a systematic shift in RA, $\Delta RA(VST - ACS) \sim +0.''6$. In our analysis we applied the correction to ACS data.

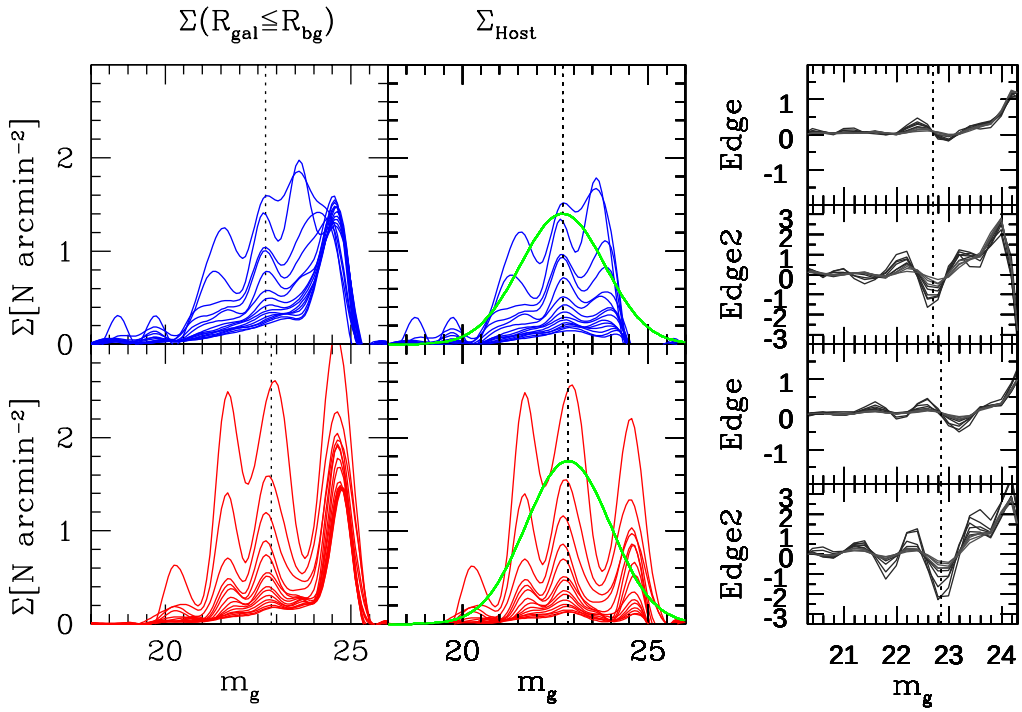

Fig. 8. GCLF for the blue and red GC components analyzed separately. The upper panels, from left to right, show the total density distribution $\Sigma(R_{gal} \leq R_{bg})$, the density after subtracting for background contamination Σ_{Host}, and the Edge and Edge2 functions. The vertical dashed line marks the approximate position of the TOM, as obtained from the Edge functions. The green line shows a Gaussian with peak at $m_g^{TOM} = 22.7$ mag. Lower panels: as upper ones, though for the red GC components, with $m_g^{TOM} = 22.85$ mag.

– axial ratio, $b/a \geq 0.3$. (van den Bergh & Morbey 1984; Blakeslee & Barber DeGraaff 2008; Cantiello et al. 2009).

Figure 10 shows the VEGAS-SSS to ACS size comparison for the full and reference samples. A first evidence is the "coma" shaped distribution of data. Such behavior highlights the expected lack of accuracy of Ishape for objects with effective radii below 1/10 the FWHM, i.e. $R_{h,VST} \lesssim 3.5$ pc at the distance of the galaxy.

If only sources in the *reference* sample and with $R_{h,ACS} \geq 3.5$ pc are used (black filled circles in Figure 10, left panels), the median ratio of ACS and VEGAS-SSS R_hs is 1.02, while rms_{MAD} (rms derived from the median absolute deviation) of the ratio is ~ 0.59. Thus, for the 29 matched objects in the *reference* sample, the median and standard deviation of the mean are 1.02 ± 0.11, providing a satisfactory agreement for the ACS and VEGAS-SSS samples when limited to the *reference* sample. Nevertheless, we must highlight that the R_h estimates for single objects can differ up to a factor $\sim$5 even for $R_{h,ACS} \geq 3.5$ pc. Further details on the differences between ACS and VEGAS-SSS size estimates for extended objects are given in Appendix C.

However, for the typical VEGAS target the selection will only rely on R_h measurements from VST images. Right panels of Figure 10 show the same data of left panels, using the $R_{h,VST}$ values for the selection instead of $R_{h,ACS}$. The ACS to VEGAS-SSS comparison worsens, as the $R_{h,ACS}$ to $R_{h,VST}$ mean ratio and standard deviation of the mean are 0.57 ± 0.06. It is interesting to note that, taking as lower limit $R_{h,VST} = 2$ pc, we obtain $\frac{R_{h,ACS}}{R_{h,VST}} = 0.78 \pm 0.08$ ($rms = 0.55$, 46 objects). This suggests that even though the nominal limit for Ishape is 1/10 the FWHM, or ~ 3.5 pc at the distance of NGC 3115, the tool allows to separate stars from extended sources down to 2 pc.

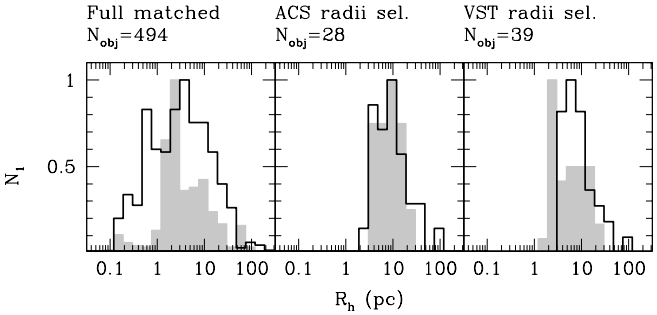

Fig. 11. R_h distribution for ACS and VEGAS-SSS samples. From left to right: R_h distribution for the full list of matched ACS and VEGAS-SSS sources, for the sample selected using $R_{h,ACS}$, and for the sample selected using $R_{h,VST}$ (see text). Shaded histograms refer to $R_{h,ACS}$ distributions, solid thick lines to $R_{h,VST}$. All histograms are normalized to one at peak value.

To further inspect the issue, Figure 11 shows the R_h distributions for: *a*) the full list of matched sources from ACS and VEGAS-SSS (left panel, ACS data in gray, VST data with thick black line), *b*) objects in the *reference* sample selected using $R_{h,ACS} \geq 3.5$ pc (middle panel), and *c*)

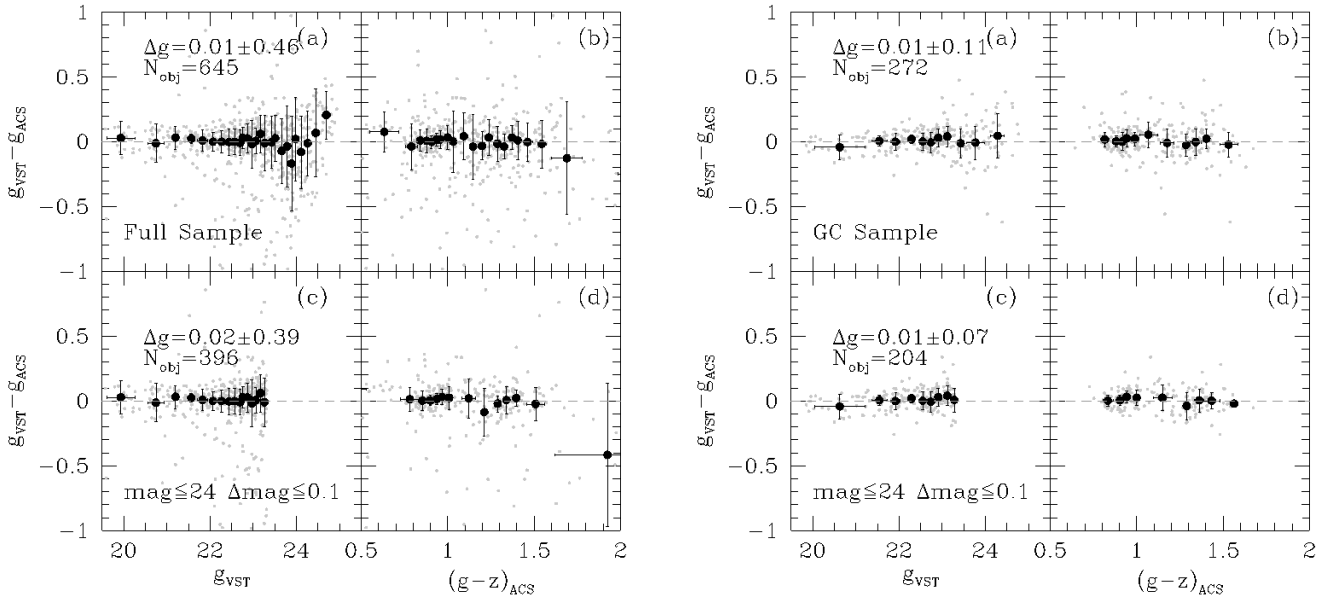

Fig. 9. Magnitude comparison between VEGAS-SSS and ACS. Left panels: (*a*) and (*b*) comparison for the full list of ACS to VEGAS-SSS matching sources (gray dots). The running mean, and the corresponding *rms*, are shown with black circles and error bars. The median difference, the *rms* and the number of objects matched are also labeled. Panels (*c*) and (*d*) same as upper panels, but for sources with magnitude and photometric error cuts as labeled. Right: as left panels, but only GC candidates in the ACS catalog are considered.

objects in the *reference* sample selected using $R_{h,VST} \geq 3.5$ pc (right panel). The ACS and VEGAS-SSS distributions appear quite similar in middle panel (case *b*). The R_h distributions based on VEGAS-SSS half-light radii (right panel, case *c*) shows a shift, with VEGAS-SSS radii being on average larger, and missing the peak at $R_h \sim 2$ pc seen in the ACS data. This behavior is due to the sources more compact than 3.5 pc, which are scattered over the entire 3.5-20 pc interval when R_h estimates from VST are used. In particular, the list of common SSS candidates in the *reference* sample goes from 28, with the selection based on the ACS radii, to 39 with the R_h selection from VST data. On such basis, we estimate that for values of $R_h \geq 3.5$ pc the *reference* sample contains $\sim 30\%$ objects with unreliable effective radii, spread over the entire R_h distribution. Needless to say that the sample of matched objects with high quality VEGAS-SSS sizes is relatively small (28 or 39, depending on the selection), thus making hard to generalize the results of the comparison over the entire VST field of view.

Finally, with the aim of deriving a catalog of GC candidates from the sole VST data, and estimating the contamination taking as *reference* the ACS GCs list, we carried out the following blind test. We adopted the selection criteria given at the beginning of this section, with the additional requirement that GC candidates must have $2 \leq R_h \leq 8$ pc (we adopted the same R_h used for GC by Jennings et al. 2014, for ACS data), and matched such VEGAS-SSS list to the sample of GC candidates from ACS. The results is that $\sim 20\%$ of the candidates (~ 10 over ~ 50) are not present in the GC list from ACS[8]. In contrast, adopting as lower limit $R_h = 3.5$ pc, the number of matching sources is ~ 30 and the contamination is nearly doubled. In other words, the test points out that the results from Ishape allow to distinguish between compact and extended sources down to $R_h = 2$ pc, although the exact value of the effective radius is reliable only above ~ 3.5 pc.

In conclusion, using the *reference* sample obtained from the coupling of photometric and spatial extent properties, the present VEGAS-SSS catalog can be used to:
i) obtain a list of GC candidates, selected in the range $2 \leq R_h(pc) \leq 8$, with an expected contamination of $\sim 20\%$, poorly populated because of the narrow selection adopted. The number of GC candidates over the entire area inspected, $\sim 52.5' \times 52.5'$ (or ~ 145 kpc $\times 145$ kpc), selected on the given photometric and size criteria is $N_{GC} \sim 220$. However, *for radii below 3.5 pc, the R_h are only used as an effective binary selection criterion* (i.e. $R_h \geq 2$ (< 2) meaning extended (point-like) source), as this limit is smaller than the nominal limit of the tool;
ii) a catalog of extended objects with $R_h \geq 3.5$ pc, having a contamination of $\sim 30\%$ objects with unreliable R_h estimates.

5.2. GC and UCD population properties based on colour and size selection criteria

Figure 12 shows the size versus magnitude diagram obtained using the *reference* sample, i.e. with the selection criteria described in the previous section, and adopting for all objects in the field the same distance modulus. In the right panel, we plotted only SSSs at galactocentric distance $R_{gal} \leq R_{bg} = 23'$, corresponding to ~ 65 kpc at the distance of NGC 3115. The approximate regions for GCs,

[8] The result is not much sensitive to the particular choices of Ishape input parameters (see Appendix B, Figure B.2).

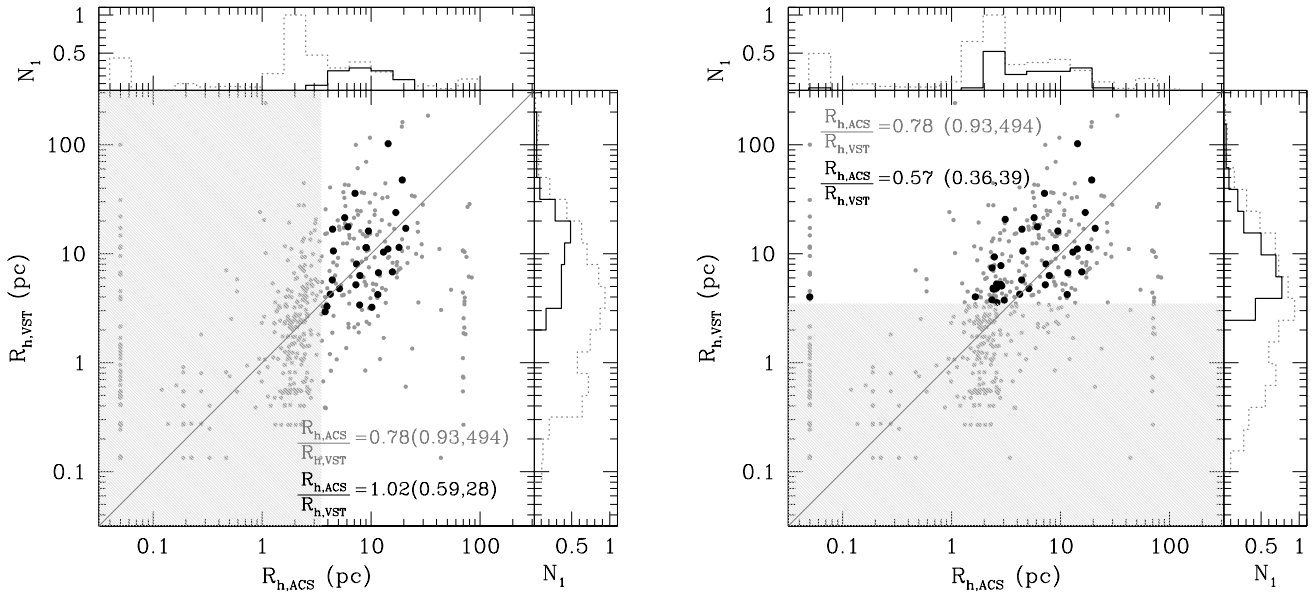

Fig. 10. Size comparison between VEGAS-SSS and ACS. Left panels: Effective radii for objects common to the ACS and VEGAS-SSS catalogs (full sample with gray dots, *reference* sample with black circles). For each sample, the median ratio between the ACS and VEGAS-SSS R_h is reported, the rms_{MAD} and the number of sources used are given in parentheses. The histograms shown in upper and right insets use the same colour coding of central panel, and are normalized to 1 at peak value for the full sample. The effective radii from ACS data are used for the selection (unshaded area). The diagonal line represents the 1:1 relation. Right panels: as left panels, but the selection is based on R_h from VEGAS-SSS.

UCDs, extended clusters (ECs), dwarf spheroidal (dSphs), dwarf ellipticals (dEs) and compact ellipticals (cEs) are shown and labeled (yellow regions; mean loci are taken from Brodie et al. 2011; Brüns & Kroupa 2012).

From Figure 12 (left panel), we find that a large fraction of selected objects in the *reference* sample falls within the avoidance region at $M_g \sim -7.5$ mag and $R_h \gtrsim 50$ pc (Forbes et al. 2013). The situation does not seem to improve much even if only sources in the *reference* sample and with SNR$\geq$ 60 (*best sample* hereafter, red circles in the figure) are considered. On the other hand, the number of sources in the avoidance area is lowered if only sources within $R_{gal} \leq R_{bg}$ are taken (Figure 12, right panel), but still significantly large. Moreover, we must highlight the large number of UCD candidates even for the *best sample* and for $R_{gal} \leq R_{bg}$ sources ($N_{UCD} = 137$).

In spite of the results by Forbes et al. (2013), who find that the avoidance zone is the result of a selection bias and confirmed the presence of various SSSs within the region, a large fraction of sources in the avoidance area are likely background galaxies (some of which are recognizable by eye). As shown by the arrow in Figure 12, in fact, a background source should move toward larger absolute radii and brighter when larger distance moduli are considered.

In right panel of Figure 12, we also plotted the GCs (green circles) and UCDs (squares) data from Jennings et al. (2014). The spectroscopically confirmed GCs and UCDs from Arnold et al. (2011) are plotted as solid symbols. Two interesting elements here are *i*) the nice overlap of the overdensity region for spectroscopically confirmed GCs and VEGAS-SSS selections, at $-7.5 \leq M_g \leq -9$ and $R_h \sim 2 - 2.5$ pc, and *b*) the presence of UCDs from the ACS sample outside the region where they typically occur. Three UCD candidates from the ACS sample, in fact, lie at $M_g \sim -9$ mag and $R_h \sim 80$ pc, i.e. within the zone of avoidance (if any). Two other UCDs have $M_g \sim -6.5$ mag and $R_h \sim 10$ pc, typically associated with the EC region (see also the discussion in Appendix C). This clearly shows that the distinction between the different SSS types is not trivial, and sometimes contains elements of arbitrariness.

To further inspect the issue, we analyzed the surface density distribution of sources versus galactocentric radius, and versus R_h. Figure 13 shows the radial surface density distribution for the *reference* and *best sample*s (black and red histograms in panel (*a*), respectively), for GC candidates ($2 \leq R_h\ (pc) \leq 8$, panel (*b*)), and for UCD candidates ($8 < R_h\ (pc) \leq 100$, panel (*c*))[9]. The gray lines in the figure show the $r^{1/4}$ profile assuming a constant background, obtained from the flat region at galactocentric radius $R_{gal} > R_{bg}$. In each panel we also report the total number of objects selected for the *reference* and *best sample* (the latter in parentheses). The surface density for the sample with no selection on sizes (panel (*a*)) shows an obvious correlation with R_{gal}, and a flattening at $R_{gal} \geq R_{bg}$, suggesting that sources beyond this radius are most likely background galaxies or foreground stars. The radial density profile for GC candidates follows a de Vaucouleurs density profile out to R_{bg}, as for the galaxy light, providing further proof to the actual membership of the objects selected to the GCs population, and supporting the role of the object-

[9] To estimate the density of sources, the effective area coverage in each annulus is corrected for the annular area outside the image and for the central uninspected regions (dashed histograms show the uncorrected distributions). Poisson statistics is adopted to estimate the errors.

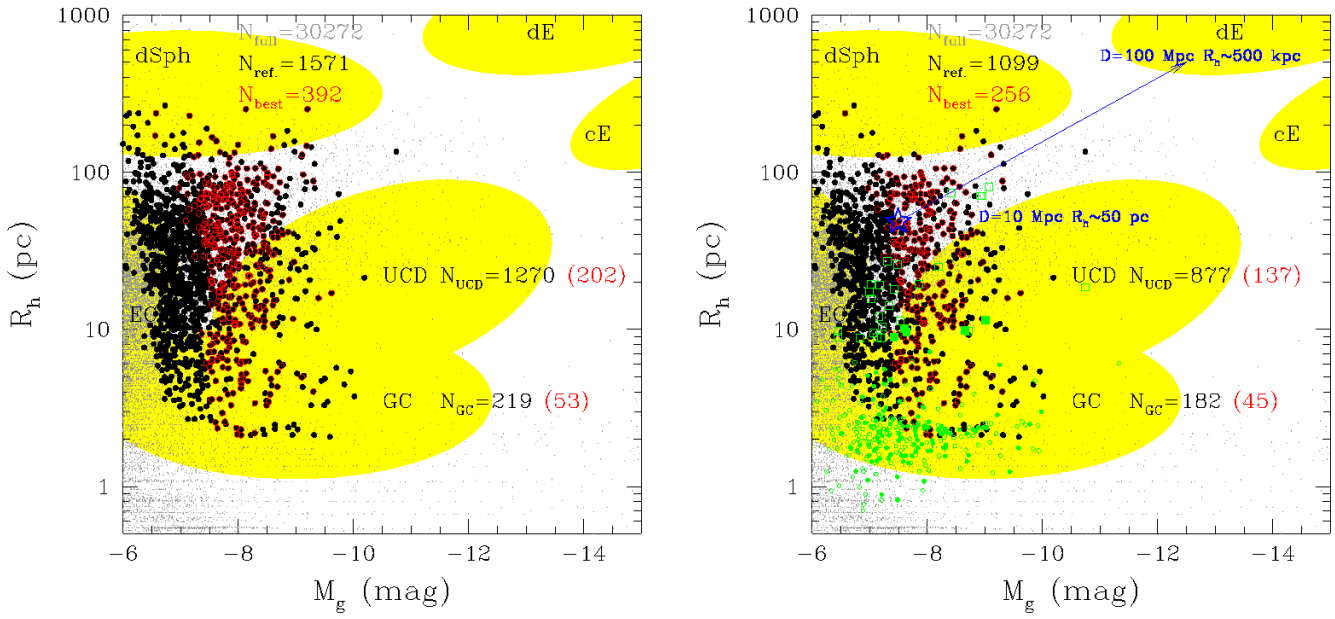

Fig. 12. Magnitude-size diagram. Left panel: magnitude versus effective radius for the VEGAS-SSS field centered on NGC 3115. Colour coding for black and gray dots is as in previous figures, with the addition of the best sample selection (red empty circles). Yellow regions show the *mean* loci of the labeled SSS classes. The number of UCD and GC candidates, N_{UCD} and N_{GC}, for the *reference* and *best sample* (given in parenthesis) are also reported. Right panel: as left panel but only sources with $R_{gal} \leq R_{bg}$ are plotted. The blue arrow shows the direction the points are shifted if the object lies at larger distance. We included the ACS sample using green symbols: GCs shown with circles, UCDs with squares. For the ACS sample, spectroscopically confirmed GCs from Arnold et al. (2011) are plotted as solid symbols.

size analysis carried out here. However, one must not neglect the presence of a fraction of background sources. For what concerns the distribution of objects with UCD-like radii, the *reference* sample does not show a tendency for a radial trend. The result is not surprising, given the small number of expected UCD-candidates and the large fraction of contaminants. It is noteworthy, though, that the UCDs in the *best sample* show hints of a radial trend.

By integrating the fitted de Vaucouleurs $r^{1/4}$ density profiles, from zero to R_{bg} for both GC and UCD density profiles, after subtracting the total number of background sources we find for the *reference* (*best*) GC sample $N_{GC} \sim 113$ (~ 42), and for the *best* UCD sample $N_{UCD} \sim 30$. The comparison of these numbers, in particular for the GCs, with the numbers in Figure 12 (right panel) confirm our previous results that the contamination for the reference GC sample is $\sim 30\%$, and also indicates that the *best sample* suffers from very small contamination. The numbers are quite different for UCDs, given the higher confusion with extended background sources. In such case, the coupling with data in other passbands will greatly reduce the contamination.

Figure 14 shows the R_h distributions for the *reference* and *best* samples, normalized to the area inspected: full detector area, objects within the $R_{gal} \leq R_{bg}$ area, objects outside $R_{gal} > R_{bg}$, and the difference between latters (from panel (a) to panel (d), respectively).

The *reference* sample over the entire VST area (upper panel), shows slightly increasing surface density for increasing R_h up to $\sim$50 pc. While the R_h distribution for the *best sample* is rather flat. The differences of the surface density for objects within R_{bg} or in the outside area, shown in panels (b) and (c) of Figure 14, are quite obvious, especially for the over-density of objects with GC-like radii, $3.5 \leq R_h\ (pc) \leq 8$. Because of the contamination, the density of sources with GC-like radii is non-zero in the outer radius (panel c). This is in part due to the expected fraction of galaxy GCs that might lie at large galactocentric distances (see Section 4), while most of the contribution comes from background contamination. Indeed, the mean density of objects with $3.5 \leq R_h\ (pc) \leq 8$ at radii $R_{gal} > R_{bg}$ (panel c) is $\sim$30% the one at $R_{gal} \leq R_{bg}$ (panel (b)). This result confirms our previous estimate of the fraction of contamination for the colour and size selected *reference* sample. Furthermore, we note that the density in the background region is $\lesssim 15\%$ the one in the inner regions for the *best sample*.

The differences between inner and outer density are better seen in panel (d) of Figure 14, where $\Delta\Sigma \equiv \Sigma(R_{gal} \leq R_{bg}) - \Sigma(R_{gal} > R_{bg})$ versus R_h is shown. Here, the surface density of sources with $R_h \gtrsim 70$ pc is consistent with zero. More in details, the $\Delta\Sigma$ distribution for the *reference* sample (black histogram), is generally consistent with zero density from $R_h \gtrsim 50$ pc (with some possible candidates at $R_h \sim 55 - 60$ pc), and for $R_h \sim 8$ pc, while for the *best sample* various regions are compatible with zero density (e.g $R_h \sim 7 - 10$ pc, $\sim 20 - 30$ pc, and ≥ 40 pc). These results, imply that the surface density of objects with such R_h values is constant over the inspected area, as would be expected from a uniform background contamination. In other words, panel (d) suggests that the majority of sources falling in the zone of avoidance (Figure 12) are background galaxies. Second, the over-abundance of sources with R_h having GCs-like radii appears clearly both for the *reference* and *best samples*. Furthermore, for the *reference* sample, we

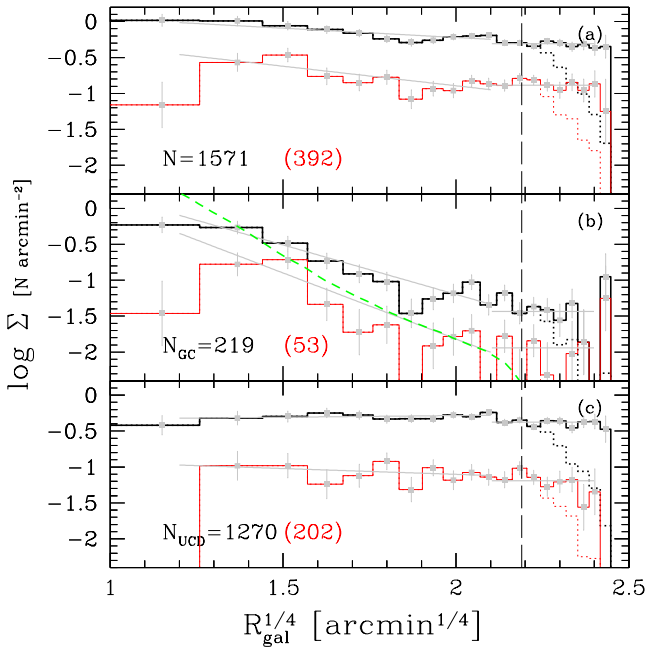

Fig. 13. Radial surface density distribution of sources in the *reference* (black histograms) and best (red histogram) samples. Panel (*a*): all R_h values are taken. The $r^{1/4}$ fit to data is shown with gray lines. The dotted lines show the histograms with no correction for areal coverage. The vertical long-dashed line is the position of limiting galactocentric radius R_{bg}. Panel (*b*): as upper, but only GC candidates are plotted. The green-dashed line shows the galaxy surface brightness (from Capaccioli et al. 2014, *g* band, arbitrary scale). Panel (*c*): as panel (*a*), but for UCD candidates.

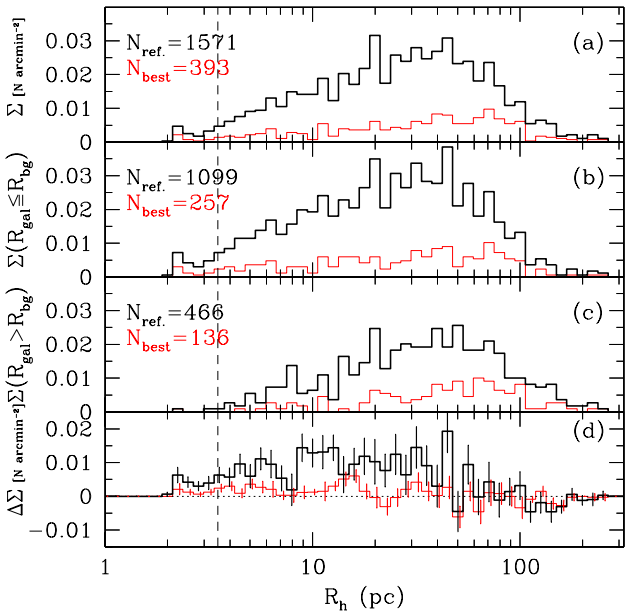

Fig. 14. R_h surface density distribution for the *reference* sample (black lines) and for the *best sample* (in red, Σ in units of number of objects per square arcminute). The panels, from upper to lower, show the surface density over the full inspected frame, for sources at $R_{gal} \leq R_{bg}$, for the background area at $R_{gal} > R_{bg}$, and for the difference between the inner and outer 23′, respectively. The vertical dashed line marks the 3.5 pc limit.

find a positive density of sources around the characteristic R_h values of UCDs (between 10 and 40 pc), which confirms the membership to this class for some of the selected objects. Such over-density, though, is weaker for the *best sample*, and possibly consistent with zero in some cases.

6. Summary

In this paper we presented the first results of the VEGAS survey for the specific science case of small stellar systems, SSSs. We described the methodology for the photometry and the size analysis of SSS candidates in the field of NGC 3115, a well studied lenticular galaxy, and showed the potential of the survey in providing original results on SSS-related science.

The VEGAS survey will collect the deep *g* and *i* imaging of bright ellipticals in the Southern hemisphere, possibly complemented with *r* for most of the targets, and also with *u* band observations for selected galaxies. One of the great advantages of VEGAS-SSS is the use of wide field imaging, ∼ 1 square degree, which allows to study the properties of SSSs out to very large galactocentric distances, with an accurate characterization of the background contaminating objects. For the specific case of NGC 3115 we inspected the properties of SSSs out to ∼ 23′, i.e. more than twenty times the effective radius of the galaxy.

We first analyzed the properties of the GCs system. Being the population of SSSs numerically most abundant in the galaxy, GCs properties can be derived using the sole photometric information, colour and magnitudes, by comparing the surface density of sources in the inner galaxy regions with the density in the outer regions. Our results can be roughly divided into two groups: *i*) results that repeat previous analysis, giving us the chance to confirm the reliability of this study; *ii*) new results allowed by the use of the wide-field imaging. In the first group we include:

- the GCs have a bimodal $(g-i)$ distribution with peaks at ∼ 0.75 and ∼ 1.0 mag;
- red GCs are more centrally concentrated than blue GCs;
- as for the galaxy light, the radial density of GCs follows a de Vaucouleurs $r^{1/4}$ profile, but with a shallower slope.
- the turnover magnitude of the *g*-band GCLF, M_g^{TOM}, coupled with the calibration from the ACSVCS survey, implies a distance modulus $\mu_0 = 29.95 \pm 0.3$ in good agreement with the literature.

Such achievements support the results of previous studies, some of which carried out with 8-10m class telescopes, and are further complemented by the following compelling results:

- the colour bimodality extends to more than ∼ 20 galaxy effective radii;
- the blue GCs show a tendency towards bluer colour at larger galactocentric radii R_{gal}, while red GCs seem to have a nearly constant colour with R_{gal};
- the galaxy light has a steeper density profile than the GCs, whether the blue or total fractions of GCs is taken into account;

- the slope of the surface density profile for red GCs at $R_{gal} \geq 7.5'$ matches with that for the galaxy light, while a red GCs overdensity appears in the inner galaxy regions;
- the ratio of blue to red clusters shows a trend with R_{gal}, with the fraction of blue GCs being slightly larger at larger radii;
- by analyzing separately the blue and red GCs we find a $\Delta m_g^{TOM} \sim 0.2$ mag, with the blue TOM being brighter;
- we do not find an obvious dependence of M_g^{TOM} with R_{gal}.

Both the colour and luminosity properties obtained are consistent with similar existing studies of the GC system in other early-type galaxies.

The presence of a bimodal GC system, with blue GCs more extended than the galaxy stellar light, and a deficiency of red GCs in the inner regions, have already been observed in other early-type galaxies brighter than NGC 3115, and support a scenario where blue GCs are associated with the galaxy halo, while red ones are more centrally concentrated and associated with the bulge stellar component in the galaxy. The overall observed properties might suggest that the galaxy has undergone a relatively quiescent evolution, without major star-forming events.

Adding the spatial extent of the sources to the colour information gives a further criterion for selecting SSSs, in particular GCs and UCDs. We used Ishape to determine the effective radius R_h of slightly extended objects in the field. By comparing our estimates for the objects in the *reference* sample with the ones in the literature, obtained from ACS data, we find on average satisfactory agreement. However, the R_h estimates for single objects can differ up to a factor $\sim$5 between ACS and VEGAS-SSS. Furthermore, the result is sensitive to the R_h estimate taken as reference (ACS or VEGAS-SSS), because of the contamination of the VEGAS-SSS sample. The various comparisons with the literature and with inner/outer galaxy regions suggest that the level of fore/background contamination of our *reference* sample is $\sim$ 30%, possibly reduced to one half for the (poorer) *best sample*. Future studies with new VEGAS-SSS u and r band data will be used to further constrain the properties of other, less populated classes of SSSs, like cEs, in the field of NGC 3115.

In spite of the large uncertainties posed by the estimate of R_h, the results obtained are encouraging, suggesting that similar analysis could be successfully carried out for the other targets in the survey. Although, at larger distances, the study of sizes will be limited to the most extended SSSs (UCDs, cEs), excluding the GCs component for most of the targets beyond $\sim$ 10 Mpc distance.

The results of this work, on one hand confirm the existing studies, thus support the validity of the analysis scheme developed here using data from the 2.6m VST telescope. On the other hand they provide new and independent results - especially for what concerns the GCs properties out to the previously unreached galactocentric distance of $\sim$ 65 kpc - showing the great potential for future applications to other VEGAS targets, in particular for the part of the sky not accessible to similar facilities.

As a final remark, we highlight that, at survey completion, for most of the VEGAS targets observations in at least one more passband other than g and i will be available. The selection of SSSs with a further optical color would certainly reduce the percentage of contaminants, especially if u band photometry is included. However, a contamination free catalog based on purely optical photometry is basically unattainable. Since the coupling of optical data with just one near-IR band is very effective in reducing the fraction of contaminants to the GC and UCD populations to $\lesssim 5\%$, the VEGAS-SSS catalogs will be perfectly suited to be complemented with single-band near-IR imaging (e.g. with a large format near-IR imager like VISTA), to define the most complete and clean SSS catalogs possible, essential for, e.g., future spectroscopic follow-up.

Acknowledgements. The optical imaging is collected at the VLT Survey Telescope using the Italian INAF Guaranteed Time Observations. The data reduction for this work was carried out with the computational infrastructures of the VST Center at Naples (VSTceN). We gratefully acknowledge INAF for financial support to the VSTceN. Part of this work was supported by PRIN-INAF 2011 (P.I.: G. Marconi), FIRB-MIUR 2008 (P.I. G. Imbriani), PRIN-INAF 2011 (P.I.: A. Grado). M.P. acknowledges finical support from project FARO 2011 from the University of Naples Federico II. D.A.F. thanks the ARC for financial support via DP130100388. We are grateful to John P. Blakeslee, and Zach Jennings for useful discussions related to this work. This research has made use of the NASA/IPAC Extragalactic Data-base (NED) which is operated by the Jet Propulsion Laboratory, California Institute of Technology, under contract with the National Aeronautics and Space Administration. This research has also made use of the SIMBAD database, operated at CDS, Strasbourg, France, and of the HyperLeda database (http://leda.univ-lyon1.fr).

References

Alamo-Martínez, K. A., West, M. J., Blakeslee, J. P., et al. 2012, A&A, 546, A15
Arnold, J. A., Romanowsky, A. J., Brodie, J. P., et al. 2011, ApJ, 736, L26
Ashman, K. M., Conti, A., & Zepf, S. E. 1995, AJ, 110, 1164
Ashman, K. M. & Zepf, S. E. 1992, ApJ, 384, 50
Bassino, L. P., Muzzio, J. C., & Rabolli, M. 1994, ApJ, 431, 634
Bernstein, R. A., Freedman, W. L., & Madore, B. F. 2002, ApJ, 571, 107
Bertin, E. & Arnouts, S. 1996, A&AS, 117, 393
Blakeslee, J. P. & Barber DeGraaff, R. 2008, AJ, 136, 2295
Blakeslee, J. P., Cantiello, M., & Peng, E. W. 2010, ApJ, 710, 51
Blom, C., Spitler, L. R., & Forbes, D. A. 2012, MNRAS, 420, 37
Brodie, J. P., Romanowsky, A. J., Strader, J., & Forbes, D. A. 2011, AJ, 142, 199
Brodie, J. P., Romanowsky, A. J., Strader, J., et al. 2014, ArXiv e-prints
Brodie, J. P. & Strader, J. 2006, ARA&A, 44, 193
Brodie, J. P., Usher, C., Conroy, C., et al. 2012, ApJ, 759, L33
Brüns, R. C. & Kroupa, P. 2012, A&A, 547, A65
Cantiello, M., Blakeslee, J. P., & Raimondo, G. 2007, ApJ, 668, 209
Cantiello, M., Blakeslee, J. P., Raimondo, G., et al. 2014, A&A, 564, L3
Cantiello, M., Blakeslee, J. P., Raimondo, G., et al. 2005, ApJ, 634, 239
Cantiello, M., Brocato, E., & Blakeslee, J. P. 2009, A&A, 503, 87
Cantiello, M., Brocato, E., & Capaccioli, M. 2011, A&A, 534, A35
Capaccioli, M., Held, E. V., & Nieto, J.-L. 1987, AJ, 94, 1519
Capaccioli, M. & Schipani, P. 2011, The Messenger, 146, 2
Capaccioli et al., M. 2014, in preparation
Caso, J. P., Bassino, L. P., Richtler, T., Smith Castelli, A. V., & Faifer, F. R. 2013, MNRAS, 430, 1088
Chiboucas, K., Tully, R. B., Marzke, R. O., et al. 2011, ApJ, 737, 86
Côté, P., Marzke, R. O., & West, M. J. 1998, ApJ, 501, 554
D'Abrusco, R., Fabbiano, G., Mineo, S., et al. 2014, ApJ, 783, 18
D'Abrusco, R., Fabbiano, G., Strader, J., et al. 2013, ApJ, 773, 87
Di Criscienzo, M., Caputo, F., Marconi, M., & Musella, I. 2006, MNRAS, 365, 1357
Dirsch, B., Richtler, T., Geisler, D., et al. 2003, AJ, 125, 1908
Dirsch, B., Schuberth, Y., & Richtler, T. 2005, A&A, 433, 43

Drinkwater, M. J., Gregg, M. D., Couch, W. J., et al. 2004, PASA, 21, 375
Duc, P.-A. 2014, ArXiv e-prints
Durrell, P. R., Côté, P., Peng, E. W., et al. 2014, ArXiv e-prints
Faifer, F. R., Forte, J. C., Norris, M. A., et al. 2011, MNRAS, 416, 155
Ferrarese, L., Côté, P., Cuillandre, J.-C., et al. 2012, ApJS, 200, 4
Forbes, D. A., Brodie, J. P., & Grillmair, C. J. 1997, AJ, 113, 1652
Forbes, D. A., Pota, V., Usher, C., et al. 2013, MNRAS, 435, L6
Forbes, D. A., Sánchez-Blázquez, P., Phan, A. T. T., et al. 2006, MNRAS, 366, 1230
Forbes, D. A., Spitler, L. R., Strader, J., et al. 2011, MNRAS, 413, 2943
Forte, J. C., Faifer, F., & Geisler, D. 2005, MNRAS, 357, 56
Galleti, S., Federici, L., Bellazzini, M., Fusi Pecci, F., & Macrina, S. 2004, A&A, 416, 917
Goudfrooij, P., Schweizer, F., Gilmore, D., & Whitmore, B. C. 2007, AJ, 133, 2737
Grado, A., Capaccioli, M., Limatola, L., & Getman, F. 2012, Memorie della Societa Astronomica Italiana Supplementi, 19, 362
Hanes, D. A. & Harris, W. E. 1986, ApJ, 304, 599
Harris, W. E. 1991, ARA&A, 29, 543
Harris, W. E. 1996, AJ, 112, 1487
Harris, W. E. 2001, in Saas-Fee Advanced Course 28: Star Clusters
Harris, W. E., Kavelaars, J. J., Hanes, D. A., Hesser, J. E., & Pritchet, C. J. 2000, ApJ, 533, 137
Harris, W. E. & van den Bergh, S. 1981, AJ, 86, 1627
Huxor, A. P., Mackey, A. D., Ferguson, A. M. N., et al. 2014, MNRAS, 442, 2165
Huxor, A. P., Tanvir, N. R., Irwin, M. J., et al. 2005, MNRAS, 360, 1007
Jedrzejewski, R. I. 1987, MNRAS, 226, 747
Jennings, Z. G., Strader, J., Romanowsky, A. J., et al. 2014, AJ, 148, 32
Jordán, A. 2004, ApJ, 613, L117
Jordán, A., McLaughlin, D. E., Côté, P., et al. 2007, ApJS, 171, 101
Jordán, A., Peng, E. W., Blakeslee, J. P., et al. 2009, ApJS, 180, 54
Karachentsev, I. D., Sharina, M. E., Dolphin, A. E., et al. 2001, A&A, 375, 359
Kartha, S. S., Forbes, D. A., Spitler, L. R., et al. 2013, MNRAS
King, I. 1962, AJ, 67, 471
Kissler-Patig, M. 1997, A&A, 319, 83
Kuijken, K. 2011, The Messenger, 146, 8
Kundu, A. & Whitmore, B. C. 1998, AJ, 116, 2841
La Barbera, F., de Carvalho, R. R., Kohl-Moreira, J. L., et al. 2008, PASP, 120, 681
Larsen, S. S. 1999, A&AS, 139, 393
Larsen, S. S. & Brodie, J. P. 2000, AJ, 120, 2938
Larsen, S. S. & Brodie, J. P. 2003, ApJ, 593, 340
Larsen, S. S. & Richtler, T. 2000, A&A, 354, 836
Lee, M. G. 1993, ApJ, 408, 409
Liu, C., Peng, E. W., Jordán, A., et al. 2011, ApJ, 728, 116
Madrid, J. P. 2011, ApJ, 737, L13
McConnachie, A. W. 2012, AJ, 144, 4
Mieske, S., Hilker, M., Infante, L., & Jordán, A. 2006, AJ, 131, 2442
Mieske, S., Hilker, M., & Misgeld, I. 2012, A&A, 537, A3
Misgeld, I. & Hilker, M. 2011, MNRAS, 414, 3699
Misgeld, I., Hilker, M., & Mieske, S. 2009, A&A, 496, 683
Muñoz, R. P., Puzia, T. H., Lançon, A., et al. 2014, ApJS, 210, 4
Muratov, A. L. & Gnedin, O. Y. 2010, ApJ, 718, 1266
Norris, M. A., Gebhardt, K., Sharples, R. M., et al. 2012, MNRAS, 421, 1485
Norris, M. A., Sharples, R. M., & Kuntschner, H. 2006, MNRAS, 367, 815
Peng, E. W., Côté, P., Jordán, A., et al. 2006, ApJ, 639, 838
Peng, E. W., Ford, H. C., Freeman, K. C., & White, R. L. 2002, AJ, 124, 3144
Peng, E. W., Jordán, A., Blakeslee, J. P., et al. 2009, ApJ, 703, 42
Puzia, T. H., Kissler-Patig, M., Brodie, J. P., & Huchra, J. P. 1999, AJ, 118, 2734
Puzia, T. H., Kissler-Patig, M., Brodie, J. P., & Schroder, L. L. 2000, AJ, 120, 777
Puzia, T. H., Paolillo, M., Goudfrooij, P., et al. 2014, ApJ, 786, 78
Puzia, T. H. & Sharina, M. E. 2008, ApJ, 674, 909
Puzia, T. H., Zepf, S. E., Kissler-Patig, M., et al. 2002, A&A, 391, 453
Rejkuba, M., da Costa, G. S., Jerjen, H., Zoccali, M., & Binggeli, B. 2006, A&A, 448, 983
Schlafly, E. F. & Finkbeiner, D. P. 2011, ApJ, 737, 103
Schlegel, D. J., Finkbeiner, D. P., & Davis, M. 1998, ApJ, 500, 525
Tonini, C. 2013, ApJ, 762, 39
Tonry, J. L., Dressler, A., Blakeslee, J. P., et al. 2001, ApJ, 546, 681
Tyson, J. A. 1988, AJ, 96, 1
Usher, C., Forbes, D. A., Brodie, J. P., et al. 2012, MNRAS, 426, 1475
van den Bergh, S. & Morbey, C. L. 1984, ApJ, 283, 598
Vanderbeke, J., West, M. J., De Propris, R., et al. 2014, MNRAS, 437, 1725
Vesperini, E. 2001, MNRAS, 322, 247
West, M. J., Cote, P., Jones, C., Forman, W., & Marzke, R. O. 1995, ApJ, 453, L77
Whitmore, B. C., Sparks, W. B., Lucas, R. A., Macchetto, F. D., & Biretta, J. A. 1995, ApJ, 454, L73
Yoon, S.-J., Lee, S.-Y., Blakeslee, J. P., et al. 2011, ApJ, 743, 150

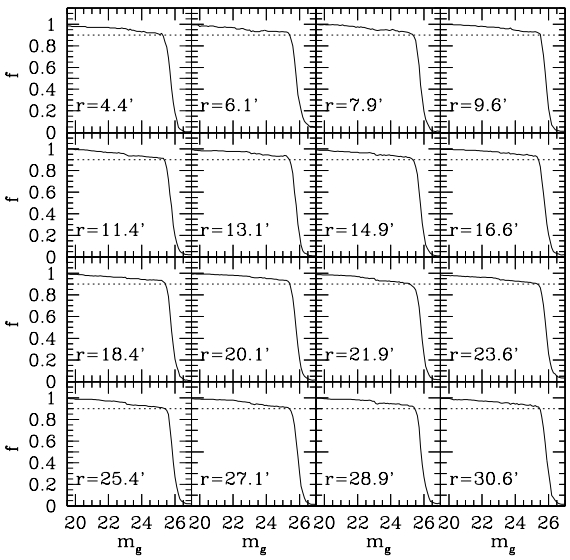

Fig. A.1. Completeness function estimated at different galactocentric radii. The label refers to the mean radius of the annulus in arcminutes. The dotted lines show the 90% completeness limit.

Appendix A: On the completeness and the edge detection functions

Appendix A.1: Completeness correction

The completeness function of the g-band images was determined by adding artificial stars to the original images and then reprocessing them as described in Section 3. The ratio between the number of artificial stars added, and the number of stars recovered provides the estimate of the completeness. We added stars using a grid pattern, with $\sim 20''$ increments in x and y. Since the field is dominated by the light from NGC 3115, the correction for magnitude completeness depends on the angular distance from the galaxy center (e.g. Cantiello et al. 2007). The radial dependent completeness function is shown in Figure A.1. To correct the luminosity functions the number of objects at given magnitude is multiplied by $1/f$ using the proper function at each galactocentric distance.

Appendix A.2: Edge detection filter

In Figure A.2 we analyze the behavior of the edge-detection function on a composite function similar to the one expected for the sources in the field of NGC 3115. The function inspected is the sum of a gaussian GCLF (Harris 2001) and a power law for background galaxies (Tyson 1988; Bernstein et al. 2002), times a completeness smoothed step function (green, blue and red line, respectively). The edge-detection function, in a first approximation, is a derivative function and shows an inflection point at the GCLF turnover magnitude (Figure A.2, middle panel). A second run of the edge function - Edge2, roughly a second derivative - reaches a local extrema at the TOM. Thus, in first approximation, the turnover of the GCLF can be found in

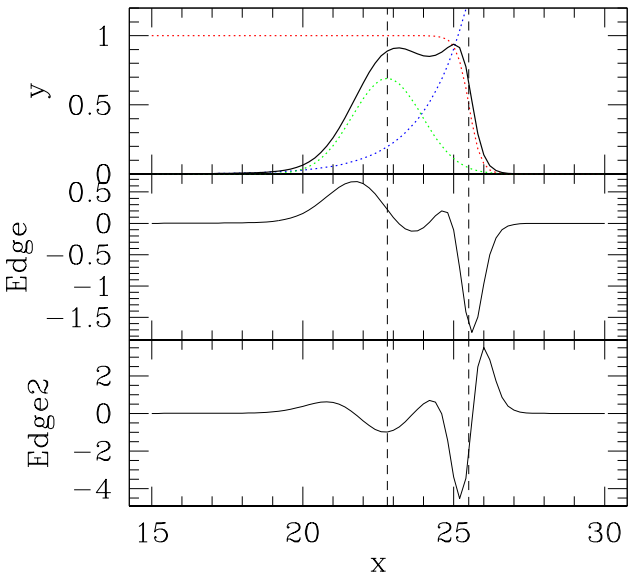

Fig. A.2. Upper panel: analytic GCLF (green line), background galaxies (blue), and completeness function (red) are combined in the total expected total luminosity function (black solid line). The GCLF peak (at x=22.8), and 50% completeness limit (at x=25.5) are shown with dashed vertical lines. Middle panel: edge detection function applied to the analytical formula of the total luminosity function. Lower panel: second-run edge detection.

correspondence of an inflection and a local extrema in the Edge and Edge2 functions, respectively.

Appendix B: Some details on Ishape

Ishape uses a PSF subsampled by a factor 10 relative to the resolution of the science image. To model the PSF we used the DAOPHOT package within IRAF and, to reduce the chance of contaminating the PSF modeling with GCs in the galaxy, we included in the list of PSF candidates unsaturated sources with $g{-}i \leq 0.3$, $g{-}i \geq 1.7$ and $m_g \geq 18$ mag. To account for PSF variations across the image, we set DAOPHOT VARORDER=2, which means that the PSF is quadratically variable over the image. Then, the frame was divided in a grid of 5×5 equal subframes, and the model PSF for Ishape evaluated in the center of each subframe.

Within Ishape, we adopted the "KING30" profile, i.e. the King (1962) model with concentration parameter $c = 30$, which is typical for marginally resolved GCs and UCDs (Larsen & Richtler 2000; Blakeslee & Barber DeGraaff 2008).

In order to determine the best parameters for Ishape we performed a reference run and various tests changing the input parameters. Table B.1 gives the main parameters for the reference run (g1 label). The other tests are obtained as follows: test#1 we adopted the DAOPHOT Penny1 PSF instead of the Moffat25 (label g2); for test#2 and #3 (labels g3 and g4) we used Ishape fitting radius 9 pixels and 15 pixels, respectively; test#4: the maximum FWHM is set to 40 pixels (label g5); test#5: does not fit an elliptical model, circular symmetry is used instead (label g6). In all cases,

Table B.1. Main Ishape parameters used for the analysis.

Parameter	Value	Explanation
PSF	Moffat25	Input PSF from DAOPHOT
FITRAD	12	Fitting radius
CENTERRAD	3	Maximum centering radius
CLEANRAD	3	Cleaning radius
CTRESH	2	Threshold for cleaning
MAXCITER	5	Maximum number of iterations
CENTERMETHOD	MAX	Centering method
SHAPE	KING30	Shape used for profile fitting
FWHMMAX	20.0	Maximum FWHM
ITMAX	200	Maximum number of iterations
ELLIPTICAL	YES	Use elliptical model
EPADU	11.5	$e-$/ADU conversion factor
RON	7.0	CCD read-out noise
CALCERR	YES	Calculate errors

except for the test #6, the FWHM is transformed to circularized effective radius $R_h = 1.48 \cdot FWHM_{KING30} \cdot 0.5 \cdot (1+w_y/w_x)$, where $FWHM_{KING30}$ and w_y/w_x are the full width, and the axis ratio fitted by Ishape[10]. For the test #6 we used $R_h = 1.48 \cdot FWHM_{KING30}$. Figure B.1 shows the results of the Ishape tests. The data in the figure show that, in general, there can be even a factor 10 difference between R_h estimates with different Ishape input parameters. Nevertheless, for the *reference* sample (see Section 5), the effect of changing fitting parameters implies a median change on R_h of $\lesssim 10\%$. We also inspected the correlation between the radius and magnitude of the sources, and did not find any.

Figure B.2 shows the VEGAS-SSS to ACS comparison for the various tests. The data in the figure show that the results with the reference g1 run are broadly consistent with the other tests. We note that, in choosing the best parameters for Ishape, we also took into account the number of sources successfully analyzed by the tool. For the g1 test the input catalog contained ~ 47000 sources, and the spatial parameters were obtained for ~ 30000. Such number can decrease significantly for other choices of the input parameters – most notably in the test g4.

Appendix C: On some UCDs in Jennings et al. (2014)

As discussed in Section 5, and shown in Figure 9, we found a good match with ACS photometry. Figure C.1 shows that the photometric matching is not as good for some of the UCD candidates in Jennings et al. catalog (empty circles). The mismatch cannot be simply explained by the different aperture correction, since, as described in Jennings et al. (2014, Section 2.4.1), the largest aperture correction is 0.94 mag, and we find differences up to ~ 2 mag.

To understand what the issue is, we downloaded one of the ACS pointings of NGC 3115 (choosing the one maximizing the number of UCDs over the frame), and independently derived the photometry of SSSs candidates using the same methods and tools described in Section §3. Figure C.2 shows the comparison VEGAS-SSS magnitudes (g_{VST}), with our photometry from ACS images ($g_{ACS\ tw}$), and with Jennings et al. (2014) ($g_{ACS\ J14}$). From the latter

[10] This equation, suggested in the Ishape handbook, provides results nearly identical to the one $R_h = 1.48 \cdot FWHM_{KING30} \cdot \sqrt{w_y/w_x}$ used by other authors (e.g. Blakeslee & Barber DeGraaff 2008).

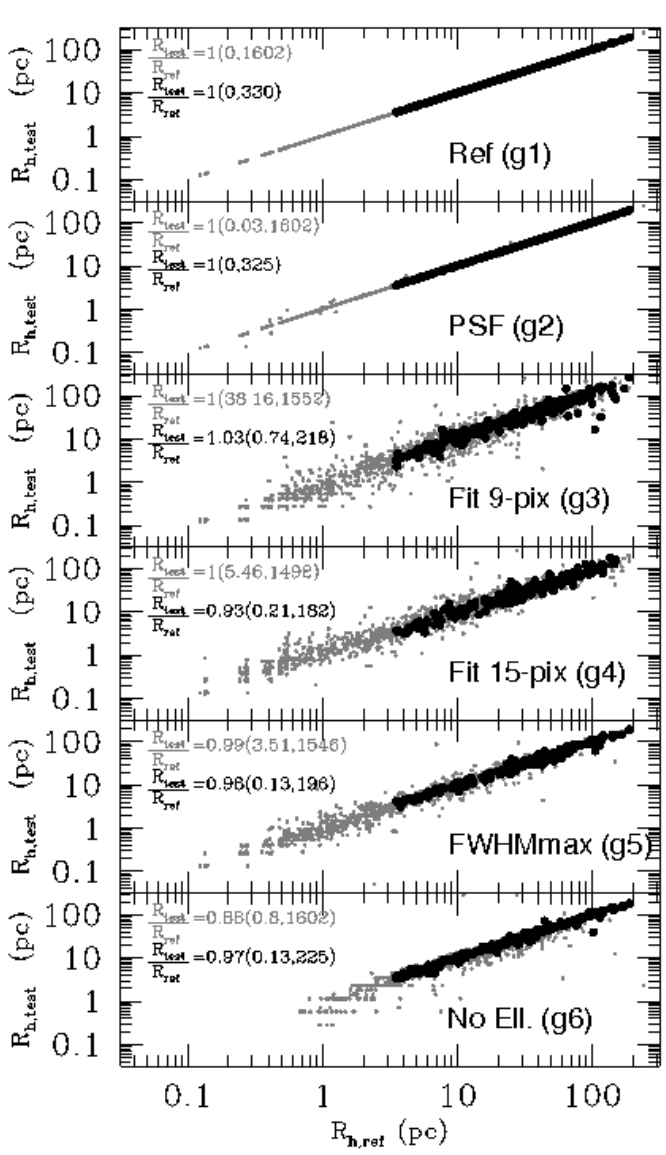

Fig. B.1. Comparison of effective radii with different Ishape input parameters. Grey circles refer to the full list of matched sources, black dots the *reference* sample. The numbers in each panel show the median $R_{h,test}/R_{h,ref}$ ratio, with the rms_{MAD} and the number of objects used in parenthesis, labels are colour coded.

test, we find that, while the agreement for GC photometry is still acceptable, the large difference between ACS and VEGAS-SSS UCD data disappears (right panel in the figure). The large scatter for the GCs is mainly due to the use of only one of the ACS pointings available.

As a further check, for the UCDs in common with the ACS pointing analyzed, we also compared magnitudes and effective radii for VEGAS-SSS, using a different photometric tool, 2Dphot (La Barbera et al. 2008, test kindly carried out by F. La Barbera), and found a good matching between the results of our standard procedures and the ones from 2Dphot (Figure C.3, upper right and lower panels).

A visual inspection of some UCD candidates from Jennings et al. (2014) reveals possible problems with the

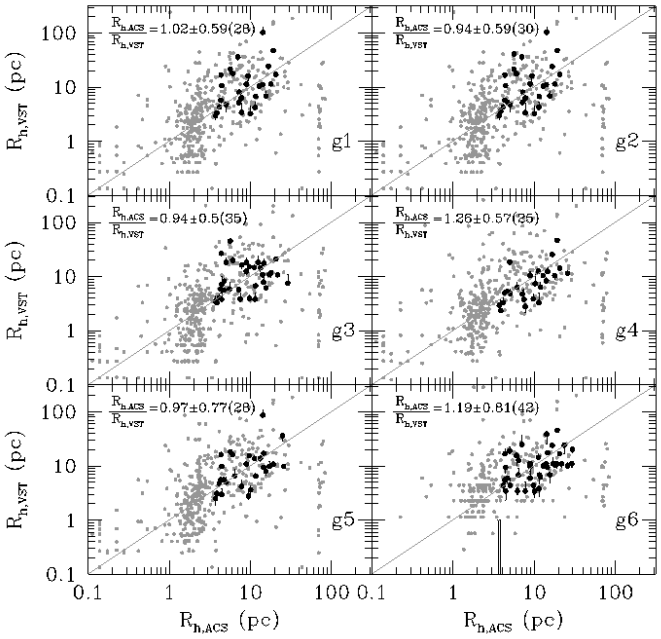

Fig. B.2. As in left panel of Figure 10, but for the different Ishape tests (as labeled).

identification of sources. The cases shown, infact, reveal that UCD10 (the object with the largest difference in the Figures C.1-C.2) and UCD20 from the Jennings et al. list, are actually a spiral galaxy and an object immersed in system with clear merging features (tidal streams?).

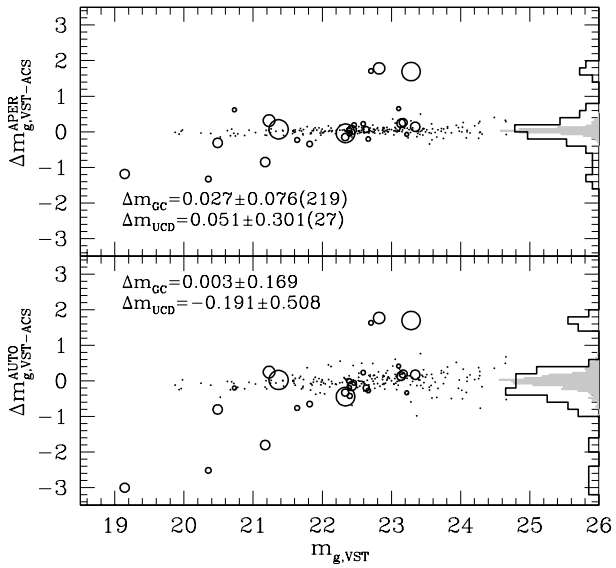

Fig. C.1. Upper panel: comparison of ACS and VEGAS-SSS aperture corrected magnitudes for the GCs and UCDs. Dots and shaded histogram refer to GCs, UCDs are shown with empty circles (with symbol size scaled to R_h) and thick solid line histogram. The number of matched sources is reported together with the median and *rms* of the VEGAS-SSS to ACS m_g difference. Lower panel: as upper but the SExtractor AUTO magnitude is used for both GCs and UCDs.

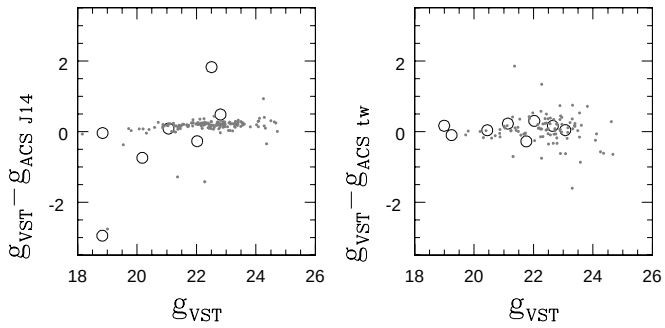

Fig. C.2. A comparison of VEGAS-SSS g-band photometry (g_{VST} label), with our photometry of ACS data ($g_{ACS\ tw}$), and with Jennings et al. (2014) measurements ($g_{ACS\ J14}$). UCDs are shown with empty circles, GCs with dots. Left panel shows the mismatch for UCDs between VEGAS-SSS and ACS measurements from Jennings et al. (2014). Right panel: as left, but our measures for the ACS pointings are used.

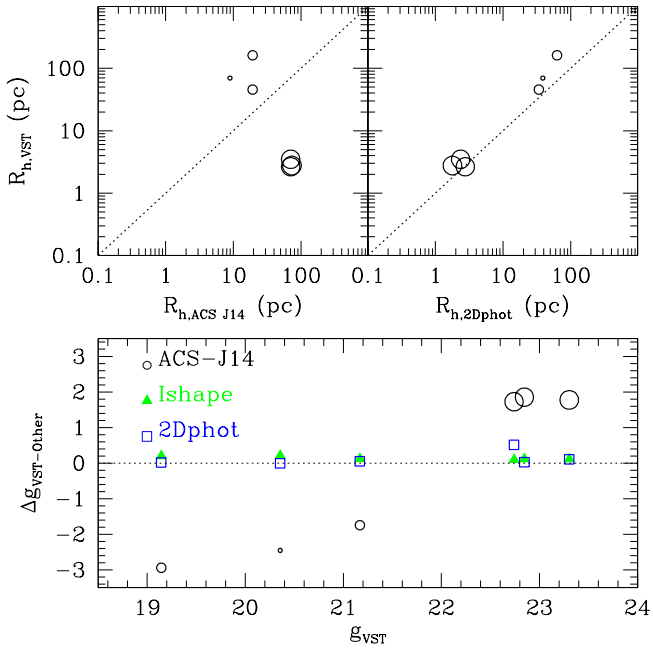

Fig. C.3. Upper panels: comparisons of effective radii for UCD candidates obtained by Jennings et al. (2014) and VEGAS-SSS results. Upper left panel: comparison between VEGAS-SSS and ACS sizes from Jennings et al. (2014). Upper right panel: comparison between the R_h from VEGAS-SSS, and measurements with 2Dphot. Lower panel: photometric comparison for the same UCDs in upper panels. VEGAS-SSS photometry is taken as *reference*. The difference with respect to ACS data from Jennings et al. (2014), magnitudes derived with Ishape, and magnitudes from 2Dphot are shown with black circles, green triangles, and blue empty squares respectively. In all panels symbols size are scaled to the R_h from Jennings et al. (2014).

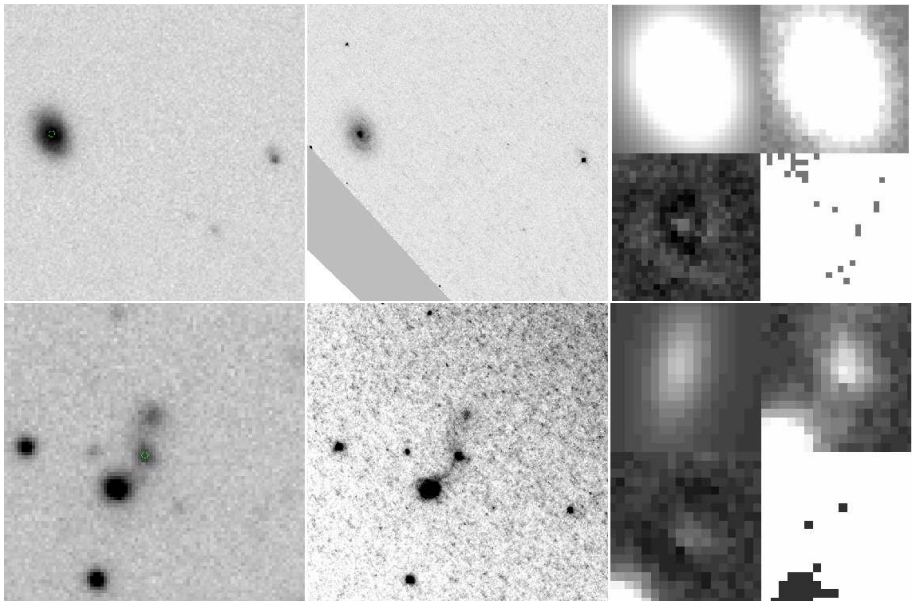

Fig. C.4. Two examples of UCD in common with Jennings et al. (2014) showing large photometric scatter with respect to VEGAS-SSS. Left/middle panel: VST/ACS g image. Right panel: lshape residual cutout. The UCD candidate is highlighted with green circle in the VEGAS-SSS panels. Upper/lower panels refer to UCD10/UCD20 in the catalog ($15''/10''$ zoom box, respectively).